Davik, Ingebrigt Eriksen

Large-Scale Numerical Modeling of Swell Waves in Bjørnafjorden Using the Phase-Resolving Wave Model REEF3D

Master's thesis in Civil and Environmental Engineering

Supervisor: Bihs, Hans

July 2020

Master's thesis

NTNU
Norwegian University of Science and Technology
Faculty of Engineering
Department of Civil and Environmental Engineering

NTNU
Norwegian University of
Science and Technology

Davik, Ingebrigt Eriksen

Large-Scale Numerical Modeling of Swell Waves in Bjørnafjorden Using the Phase-Resolving Wave Model REEF3D

Master's thesis in Civil and Environmental Engineering
Supervisor: Bihs, Hans
July 2020

Norwegian University of Science and Technology
Faculty of Engineering
Department of Civil and Environmental Engineering

NTNU
Norwegian University of
Science and Technology

Abstract

In the field of numerical wave modeling, wave propagation over quickly varying bathymetry is often demanding. Bjørnafjorden is an excellent example of a domain where islands and skerries disrupt the propagation of waves, and the water depth changes by several hundred meters over a short horizontal distance. The popular phase-averaging wave models are struggling to simulate these rapidly varying wave parameters accurately, and phase-resolved models are therefore needed. In this study, the fully nonlinear potential flow model REEF3D::FNPF is used to simulate the wave propagation of swell waves from an offshore location to Bjørnafjorden. The aim is to present and analyze the wave conditions in the fjord, as well as comparing the results to calculations by phase-averaging wave models, and data from field measurements. Five different wave inputs with varying wave height, wave period, and main direction are imposed at the offshore boundary of the numerical model.

The governing Laplace equation is discretized by a second-order central differences method, while the higher-order WENO scheme is used for the kinematic and dynamic boundary conditions. The domain is discretized in a structured grid in the horizontal directions, while a sigma-coordinate system is used in the vertical direction. The verification of the numerical model is carried out by simplified two- and three-dimensional simulations. The grid size, the stretching factor of the vertical mesh, and the distance of the coastline damping zone are determined to reduce numerical dispersion, numerical damping, unphysical dissipation, and artificial reflection to a neglectable amount.

For a 100-year return period, the maximum significant wave height in Bjørnafjorden is calculated to be 0.58 meters by REEF3D::FNPF, which is more than twice as high as the similar value calculated by the phase-averaged wave model SWAN. However, field measurements for 19 months show that even in this short period, the significant wave height exceeds 0.30 meters frequently. Results from REEF3D::FNPF also shows that low-frequency waves at 0.01 Hz are generated in Selbjørnsfjorden. SWAN, on the other hand, does not capture these waves. Additionally, the wave conditions in the fjord are found to be inhomogeneous.

The study concludes that REEF3D::FNPF is proven to be a stable and relatively efficient numerical wave model, which can calculate wave propagation over the challenging bathymetry of Bjørnafjord reasonably accurately. The phase-resolving wave model REEF3D::FNPF clearly shows a better correlation to measured data than the phase-averaged wave model SWAN. Still, further studies with comparison to more comprehensive field measurements are advised.

Keywords: Fully nonlinear potential flow, REEF3D, quickly varying bathymetry, phase-resolving wave model.

Acknowledgments

With the submission of this masters' thesis, my time as a graduate student at NTNU comes to a closure. Firstly, I want to express my gratitude towards the Norwegian Public Roads Administration for their support and interest in my work, and for giving me the opportunity to direct my thesis towards a project and a field of study that has intrigued me for years. I am also thankful for my supervisor, Associate Professor Hans Bihs, who has helped me with the theoretical aspect of numerical wave modeling. His effort to ensure that the computational model was functioning for every type of problem that occurred during the study is also highly appreciated.

A special thanks to my co-supervisor, Postdoctoral Fellow Weizhi Wang, who has helped me with every part of this process. I am deeply grateful for his contribution to my thesis, for always having time to discuss any problems, and for all the knowledge I have gained from him. His expertise and ability to teach have been essential for me to understand the diverse field of numerical wave modeling.

They are both members of the marine civil engineering research group at NTNU, which I have appreciated working with the last couple of years. In particular, I want to highlight the influence of Senior Researcher Arun Kamath whom I have experienced as an outstanding teacher. It was in his lectures that I got a better understanding of numerical wave modeling, and also when my interest in this topic arose.

Finally, I would like to thank my family for always supporting me and for giving me all the possibilities to succeed, and my classmates for exciting discussions and friendship throughout the years.

Contents

List of Figures

List of Tables

Nomenclature

Acronyms

CFD	Computational fluid dynamics
CFL	Courant–Friedrichs–Lewy condition
DNS	Direct numerical simulation
E39	European Route 39
ENO	Essentially non-oscillatory
FNPF	Fully nonlinear potential flow
HOS	Higher-order spectral
LES	Large eddy simulation
LS	Level set method
MPI	Message passing interface
NPRA	The Norwegian Public Roads Administration
NSE	Navier Stokes' equations
NTP	National Transport Plan
PDE	Partial differential equation
PNJ	Pierson-Neumann-James
RANS	Reynolds-averaged Navier-Stokes
SWE	Shallow-water equations
SWL	Still water level
TVD	Total Variance Diminishing

VoF	Volume of fluids
WENO	Weighted essentially non-oscillatory
WI#	Wave Input #

Symbols

$\alpha,\ \beta$	Wave breaking criteria
$\alpha_1, \alpha_2, \alpha_3$	WENO substencil denominators
β	Direction of each incident wave component
Δt	Numerical time step
Δx	Numerical grid size
ϵ	Dimensionless wave amplitude
η	Free surface elevation
Γ	Coastline
γ	Peak enhancement factor for JONSWAP spectrum
$\hat{h}$	Treshold water depth for coastline detection
ω	Angular frequency
$\omega_1, \omega_2, \omega_3$	WENO substencil weights
Φ	Velocity potential
ϕ	Convective term
$\phi(\,)$	Distance function
σ	Vertical coordinate on the sigma grid
τ	Fictitious time parameter
$\tilde{\epsilon}$	WENO regularization parameter
$_0$	Deep water parameter
a	Wave amplitude

$C_0,\ A_{ij},\ B_{ij}$	Dimensionless functions for fifth-order Stokes wave theory
CFL	Courant–Friedrichs–Lewy condition
d	Water depth, from the seabed to the still water level
g	Gravitational constant
$G()$	Pierson-Neumann-James spectrum
H	Wave height
h	Water depth, from the seabed to the water surface
H_s	Significant wave height
IS	Smoothness indicators
k	Wave number
L	Wavelength
$L()$	Spatial discretization
N	Number of wave components
n	Shape parameter for directional spreading function
n	Shape parameter
p	Pressure
$S()$	JONSWAP spectrum
T	Wave period
t	Time
T_p	Peak wave period
U	Velocity
u, v, w	Flow velocity in x, y, and z, respectively
Ur	Ursell parameter
x, y	Horizontal coordinates
z	Vertical coordinate, positive upwards, origin at still water level

Chapter 1

Introduction

1.1 Background

As part of the National Transport Plan (NTP) for 2014-2023, the E39 coastal highway project aims to build a continuous ferry-free road connection along the west coast of Norway, covering a distance of approximately 1100 km, including seven major fjord crossings. To cross these wide and deep fjords in Norway, innovative floating bridges and tunnels are proposed. A good understanding of the marine environment, especially the wave conditions, is therefore essential for safe and cost-effective designs of such floating structures.

Offshore wind farms and fish farms are other examples of how some of the industries of the future are making use of the marine environment. As a consequence of the increased attention to marine constructions, improved technology to predict the environmental impact on these structures is of great importance. Another factor is that we will experience more extreme weather in the future due to global warming, which implies that the structures need to withstand tougher waves and stronger winds [28].

A complex set of physical processes determines the wave conditions, of which the importance will vary for different domains. The atmospheric input, like wind and pressure, will lead to a transfer of energy between air and water. The physical processes of white-capping, wave breaking, and bottom friction will dissipate energy from the sea. Furthermore, a redistribution of the wave energy is the effect of nonlinear wave interaction, likewise for diffraction, shoaling, and refraction [8]. To correctly replicate these processes, could be both costly and complicated. For instance, the effect of white-capping in a wavefield is not fully understood and could, therefore, be challenging to evaluate and incorporate in a model [12].

Experiments, in-situ measurements, and numerical models are some of the applications used when trying to understand the wave propagation for varying topography. The latter is becoming increasingly more manageable with the quick development of computational infrastructure and supercomputers. Numerical wave models are proved to be reliable design tools with great flexibility and are seen to be more affordable and time-efficient than other alternatives [2]. Nevertheless, these simulations are so computationally demanding that we still need simplifications when modeling large-scale wave climate.

1.2 State-of-the-Art

1.2.1 Numerical Wave Models

Phase-averaging models, like SWAN and STWAVE, are the most common wave models used nowadays. Another name for these models is spectral wave models, the reason being that the evolution of the wave energy spectra is the basis of these models. A consequence of this statistical method is that these models will not provide local extreme values. Nevertheless, this type of wave model provides an efficient way to model large wave fields under the influence of wind. By comparing with in-situ measurements, Rusu & Soares [50] showed that the phase-averaging models, in general, provide reliable results. Mainly for deep and intermediate water, but also for many shallow coastal areas along the Portuguese coast. A critical weakness of the phase-averaged models is the lack of capability to calculate a rapid variation in wave parameters due to bathymetry, diffraction, and reflection [14], [41]. These weaknesses make phase-averaged models not suitable for modeling coastal areas with many islands and deep fjords, like the coast of Norway.

Another type of wave model is therefore needed to cope with coasts of extremely varying bathymetry, like the Norwegian coast. Phase-resolved models are models where the sea surface and the velocity field are explicitly reproduced [13]. This approach makes the models able to capture quick variations in wave parameters and to calculate local extreme values, but also computationally more demanding. Consequently, there exist different models based on different governing equations, where the complexity is varying.

The most exact and, by far, the most computationally demanding are the ones solving Navier Stokes' equations (NSE) with few assumptions. For example, direct numerical simulation (DNS), large eddy simulation (LES), and Reynolds-averaged Navier-Stokes equations (RANS). Simplifications are therefore needed to make large-scale

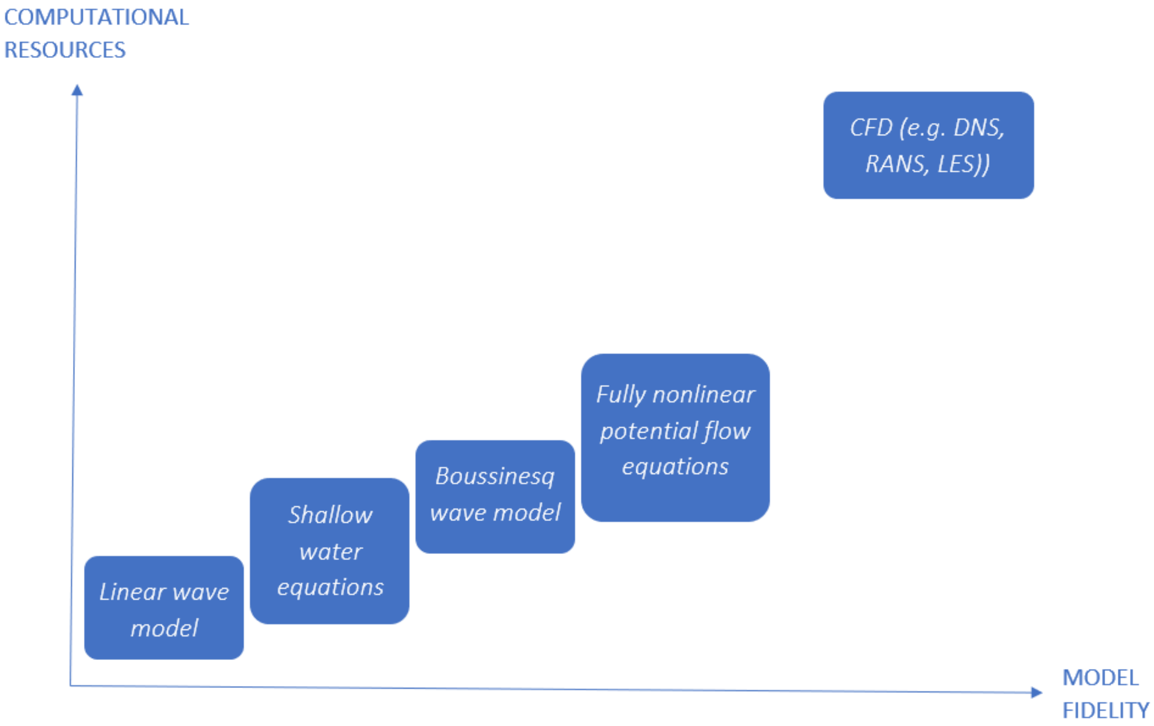

Figure 1.1: Overview of some phase-resolved wave models.

wave modeling with phase-resolved models possible. Several different approaches have been developed, all with their advantages and disadvantages. Shallow-water equation (SWE) models, Boussinesq wave models, and fully nonlinear potential flow models are all efficient phase-resolved models. This study will focus on the fully nonlinear potential flow (FNPF) model, which is closely related to the higher-order spectral (HOS) method [57], [22].

Both of these wave models solve the Laplace equation and are capable of modeling large-scale wavefields at a manageable cost. HOS models solve the nonlinear potential problem primarily for deep water, while FNPF models also are shown to simulate fast varying bathymetry accurately [11], [22]. Nevertheless, a shortcoming of these wave models is that they are constrained by empirical-based wave breaking (see Section 3.4) and wind forcing.

One way to overcome the limitations of the various wave models is to decompose the domain using different models for different parts of the domain. Such nested models make use of the strengths of each model and reduce the impact of the weaker features of the models. A logical way to decompose the domain is to utilize the spectral wave models to model the waves from offshore to the coastal areas, where a phase-resolved model takes over and simulates the waves propagating towards land. A possible

Numerical Wave Model	**Model Type**
TELEMAC-3D	Shallow water equation
FUNWAVE	Boussinesq wave model
Symphonie	Boussinesq wave model
MIKE 21	Boussinesq wave model
BOUSS-2D	Boussinesq wave model
Whispers3D	High-order spectral wave model
HOS-Ocean	High-order spectral wave model
OceanWave3D	High-order spectral wave model
OpenFOAM	Reynolds-averaged Navier–Stokes equations
3D-Flow	Reynolds-averaged Navier-Stokes equations
ANSYS-Fluent	Reynolds-averaged Navier–Stokes equations
ReFRESCO	Reynolds-averaged Navier–Stokes equations
Star CCM+	Reynolds-averaged Navier–Stokes equations
REEF3D	SWE, NSE, FNPF and RANS

Table 1.1: Examples of different phase-resolving wave models

extension will be to simulate slamming forces against a pier. A more complex computational fluid dynamics (CFD) model is therefore needed in this proposed nested wave model to simulate the small-scale wave actions at the pier.

When studying the Norwegian coast, the phase-resolved wave models are supposed to simulate wave propagation from offshore to the point of interest in the fjord. This distance could be up to 200 km. Combined with the fact that the Norwegian fjords are wide and deep, with numerous islands, cause a new set of challenges for phase-resolved wave models [23]. For more homogenous coasts, like the Danish and Portuguese, the coastal area is shorter, and the gradient of the bathymetry is usually smaller than in Norwegian fjords. Consequently, SWE models or Boussinesq wave models are often used, and wind-wave interaction is not essential compared to other physical features. On the contrary, simulations of waves in the Norwegian fjords require a wave model able to cope with the complicated bathymetry over such a vast area. Table 1.1 displays some numerical models and the governing equation of the model.

The open-source hydrodynamic model REEF3D will be used for numerical wave modeling in this work. Hans Bihs originally developed this software to solve local scouring [9]. Today, REEF3D consists of four different modules based on different sets of equations: three-dimensional Navier-Stokes equations (REEF3D::CFD), non-hydrostatic Navier-Stokes equation (REEF3D::NSEWAVE), non-hydrostatic shallow water equations (REEF3D::SFLOW), and the three-dimensional fully nonlinear potential flow solver (REEF3D::FNPF). The latter will be used in this study.

The capability of REEF3D has been demonstrated through several studies related to fluid-structure interaction [4], [34], [52] , sediment transport [3], [49], extreme waves [10], and numerical solutions [35]. Additionally, the FNPF module of REEF3D shows high accuracy when compared to experimental and theoretical data [11], [56].

1.2.2 Current Studies on Bjørnafjorden

Bjørnafjorden will be the Norwegian fjord of interest in this study. The wave climate in Bjørnafjorden has been the topic of several published studies [1], [15], [16], [17] due to the proposed fjord crossing, which is a part of the E39 coastal highway project. The Norwegian Public Roads Administration (NPRA) and DHI have measured the waves in Bjørnafjorden, and numerical studies with phase-averaging wave models have been used to get an insight into the long-term wave parameters. This section presents this measured wave data and the results from the phase-averaging models.

In the design basis from NPRA [45] for a side- and end-anchored floating bridge in Bjørnafjorden, Norconsult calculated the wave conditions with the phase-averaging wave model, STWAVE. The calculations show that the 100-year return period for the significant wave height for swell waves is 40 cm and that the impact of swell from Selbjørnsfjorden is neglectable. Even though the influence of swell is small compared to wind-generated waves, it needs to be accounted for in a situation with severe wind from the west. At the location of the proposed fjord crossing, the significant wave height is 2.8 m for a 100 year return period.

Cheng et al. [17] present and analyze measured wave data for 19 months from Bjørnafjorden. DHI measured the wave conditions along the proposed bridge. The highest record significant wave height of the recorded wave data was ranging from 1.22 m to 1.10 m for the different wave-buoys, while the peak period was 3.77 seconds for all. Swell is also present in Bjørnafjorden. However, the wave height of this type of wave is considerably smaller and rarer than wind-waves in the fjord. Out of 3250 data points, there were only 11 occurrences where the $H_s > 0.3\,m$ and $T_p > 7\,s$. It is also found that the waves appear to be inhomogenous over the cross-section of the fjord, meaning that the wave state along the proposed bridge, at the same time, will differ. Larger sway motion, axial force, and strong axis bending moment, as well as significantly larger weak axis bending moment along the bridge girder, are consequences of the bridge being exposed to inhomogeneous waves instead of homogeneous waves [16].

However, Aarnes [1] raises the concern that phase-averaging models might be underestimating both H_s and T_p for swell waves in Bjørnafjorden. In this study, two sets of measured data are compared to the results of numerical simulations with SWAN. This concern is backed by the fact that the highest recorded significant wave height for swell is 0.25 m, while the simulated $H_{s,swell}$ is below 0.02 m, especially considering that the recorded data were for three years, and the simulated time is 15 years. Hindcast data for 15 years determined the incident waves for the numerical simulation. The conclusion is that the 100-year return value estimate of significant swell wave height is approximately 0.3 m. Like the other studies, Aarnes concluded that wind-induced waves are dominating in Bjørnafjorden, and that swell coming from the northwest into Bjørnafjorden has a more significant impact than those coming from Selbjørnsfjorden.

1.3 Motivation and Objectives

The use of phase-resolving models in large-scale wave modeling is a novel approach in Norway. Due to the lack of computer resources, and because the less demanding types of phase-resolving models cannot accurately model the complex coast of Norway, the computationally efficient phase-averaging models are usually preferred. However, with increased computational resources, it is possible to utilize the advantages of the more exact phase-resolving models when modeling wave climate in Norwegian fjords. The introduction of phase-resolving models will theoretically result in more accurate results and possibly reduce safety factors in design.

The purpose of this study is to simulate the propagation of swell waves in Bjørnafjorden by using the phase-resolving wave model REEF3D::FNPF. Firstly, the properties of the incident waves and different parameters of the numerical model are determined. Furthermore, the results of the large-scale simulation are presented and analyzed to describe the wave state in Bjørnafjorden. Finally, the results provided by REEF3D are compared to field measurements and results from phase-averaging models to investigate if phase-resolved models can provide more accurate results than phase-averaging models for simulations of swell waves in Bjørnafjorden.

Chapter 2

Wave Theory

Many wave theories are implemented in REEF3D. In the following, the most relevant theories for this study are presented.

2.1 Linear Wave Theory

$$\frac{\partial u_i}{\partial x_i} = 0 \tag{2.1}$$

$$\frac{\partial u_x}{\partial t} = -\frac{1}{\rho}\frac{\partial p}{\partial x} \qquad \frac{\partial u_y}{\partial t} = -\frac{1}{\rho}\frac{\partial p}{\partial y} \qquad \frac{\partial u_z}{\partial t} = -\frac{1}{\rho}\frac{\partial p}{\partial z} - g \tag{2.2}$$

Linear wave theory is the small-amplitude approximation and applies when the wave amplitude is small compared to the water depth and wavelength. The governing equations are deduced from two fundamental equations: the mass balance equation (Eq. (2.1)), and the momentum balance equation(Eq. (2.2)). Given the small-amplitude approximation, the corresponding linearized boundary conditions are presented in Eq. (2.3) and Eq. (2.4), and is known as the kinematic boundary condition and the dynamic boundary condition, respectively [30].

$$\frac{\partial \eta(x,t)}{\partial t} = w(x,0,t) \tag{2.3}$$

$$\frac{\partial \Phi(x,0,t)}{\partial t} + g\eta(x,t) = 0 \tag{2.4}$$

η, Φ, u, w and the dispersion relation is defined as [43]:

$$\eta = a\ sin(\omega t - kx) \tag{2.5}$$

$$\Phi = \frac{ag}{\omega}\frac{cosh\ k(z+d)}{cosh\ (kd)}cos(\omega t - kx) \tag{2.6}$$

$$u = \frac{\partial \Phi}{\partial x} = \omega a \frac{cosh\ k(z+d)}{sinhkd} sin(\omega t - kx) \tag{2.7}$$

$$w = \frac{\partial \Phi}{\partial z} = \omega a \frac{sinh\ k(z+d)}{sinhkd} cos(\omega t - kx) \tag{2.8}$$

$$\omega^2 = gk\ tanh\ kd \tag{2.9}$$

2.2 Nonlinear Wave Theories

Second-Order Stokes Wave Theory

Similar to the linear wave theory, Stokes' wave theory applies to conditions where the wave height is small compared to the water depth. The theory proposes an approximation for nonlinear wave motion with the introduction of a power series of the wave steepness H/L [19]. η, Φ, u and w are defined as:

$$\eta = a\ cos(kx - \omega t) + \frac{\pi}{8}\frac{H^2}{L}\frac{cosh\ kd(2 + cosh\ 2kd)}{sinh^3\ kd} cos\ 2(kx - \omega t) \tag{2.10}$$

$$\Phi = -\frac{ag}{\omega}\frac{cosh\ k(z+d)}{cosh\ kd} sin\ (kx - \omega t) - \frac{3\pi}{16}\frac{H^2}{T}\frac{cosh\ 2k(z+d)}{sinh^4\ kd} sin\ 2(kx - \omega t) \tag{2.11}$$

$$u = -\frac{\partial \Phi}{\partial x} = \frac{agk}{\omega}\frac{cosh\ k(z+d)}{cosh\ kd} cos(kx - \omega t) + \frac{3}{16} H^2 \omega k \frac{cosh(2k(z+d))}{4T\ sinh^4\ kd} cos2(kx - \omega t) \tag{2.12}$$

$$w = -\frac{\partial \Phi}{\partial z} = \frac{agk}{\omega}\frac{sinh\ k(z+d)}{cosh\ kd} sin(kx - \omega t) + \frac{3}{16} H^2 \omega k \frac{sinh(2k(z+d))}{4T\ sinh^4\ kd} sin2(kx - \omega t) \tag{2.13}$$

Stokes' wave theory is a continuation of the linear wave theory, where Stokes waves are made of harmonic components determined by the linear wave theory. The first term in Eq. (2.10) is taken directly from the linear wave theory, while the second term is the second harmonic wave component or the second-order Stokes correction. The phase speed of the second harmonic wave component is equal to the phase speed of the first harmonic wave component, which implies that the dispersion relation is equal for linear wave theory and second-order Stokes waves [30].

The Ursell parameter is used to determine if the theory of Stokes' wave can be applied under certain conditions. If $Ur < 10$ Stokes' waves are applicable [30].

$$Ur = \frac{H\,L^2}{d^3} \tag{2.14}$$

Fifth-Order Stokes Wave Theory

The required number of terms is increasing as the wave height increases. Several theories are available for solving the expansion of the Stokes' wave theory to the fifth order, one of them being the analytical solution proposed by Fenton [27]. Fenton has obtained a solution to the fifth-order Stokes' waves based on the power series of the wave steepness to the fifth order. The resulting η, Φ, u, and w are:

$$\eta = \frac{1}{k}\sum_{n=1}^{5}\epsilon^n b_n\ cos(n\theta) \tag{2.15}$$

$$\begin{aligned} where, b_1 &= 1 + \epsilon^2 B_{31} - \epsilon^4(B_{53} + B_{55}) \\ b_2 &= B_{22} + \epsilon^2 B_{42} \\ b_3 &= -B_{31} + \epsilon^2 B_{53} \\ b_4 &= B_{44} \\ b_5 &= B_{55} \end{aligned} \tag{2.16}$$

$$\Phi = C_0\sqrt{\frac{g}{k^3}}\sum_{n=1}^{5}\epsilon^n a^n cosh(nkz) sin(n\theta) \tag{2.17}$$

$$\begin{aligned} where, a_1 &= A_{11} + \epsilon^2 A_{31} + \epsilon^4 A_{51} \\ a_2 &= A_{22} + \epsilon^2 A_{42} \\ a_3 &= A_{33} + \epsilon^2 A_{53} \\ a_4 &= A_{44} \\ a_5 &= A_{55} \end{aligned} \tag{2.18}$$

$$u = C_0\sqrt{\frac{g}{k}}\sum_{n=1}^{5}\epsilon^n\ n\ a_n cosh(nkz) cos(n\theta) \tag{2.19}$$

$$w = C_0\sqrt{\frac{g}{k}}\sum_{n=1}^{5}\epsilon^n\ n\ a_n sinh(nkz) sin(n\theta) \tag{2.20}$$

The coefficients C_0, A_{ij}, B_{ij} are dimensionless functions of the water depth h and wavelength L. The dimensionless wave amplitude is defined as:

$$\epsilon = \frac{kH}{2} \tag{2.21}$$

2.3 Irregular Wave Theory

The model is also able to generate irregular waves based on different distributions. In the large-scale simulation of this study, multi-directional first-order irregular waves are used to simulate realistic wave fields. The JONSWAP spectrum suggested by DNV-GL [21] is adopted to determine the energy at different frequencies for a fully-developed sea, while a Mitsuyasu-type spreading function [42] is used to describe the directionality of the wave components. The latter is a continuation of the original Pierson-Neumann-James (PNJ) directional spreading function [48], which is expressed in Eq. (2.25). The following equation determines the JONSWAP spectrum:

$$S\left(\omega\right) = \frac{5}{16} H_s^2 \omega_p^4 \omega^{-5} exp\left(-\frac{5}{4}\left(\frac{\omega}{\omega_p}\right)^{-4}\right) \gamma^{exp\left(\frac{-(\omega-\omega_p)^2}{2\sigma^2\omega_p^2}\right)} A_\gamma. \tag{2.22}$$

$$A_\gamma = 1 - 0.287 ln(\gamma). \tag{2.23}$$

$$\sigma = \begin{cases} 0.07 & if\ \omega \leq \omega_p \\ 0.09 & if\ \omega \geq \omega_p \end{cases} \tag{2.24}$$

where H_s is the significant wave height, ω_p is the peak angular frequency, N is the number of wave components, and the peak enhancement factor γ is typically chosen to be 3.3.

$$G(\beta_j) = \begin{cases} \frac{2}{\pi}\cos^n(\beta_j - \overline{\beta}) & ,\ if\ \ |\beta_j| < \frac{\pi}{2} \\ 0 & ,\ else. \end{cases} \tag{2.25}$$

Where $\overline{\beta}$ is the principal direction and β_j is the direction of each incident wave component measured counterclockwise from the principal direction. The shape parameter n determines the strength of the directional spreading.

2.4 Wave Transformation

Waves in water are the result of energy transferred to the water at one location and transported away to return to equilibrium, which for an idealized scenario is still water level (SWL). Energy is transferred to the water through numerous processes like the attraction of the sun and the moon (tidal waves), tectonic movement (tsunamis), and, of course, wind. The latter could be separated into two different categories: swell waves and wind waves. In general, they are the same thing; surface friction between the blowing wind and the water causes movements in the sea. The difference is where the waves are generated. Wind waves are locally formed by the wind, and the wave period is shorter compared to swell waves. Swell waves, on the other hand, are generated by the wind blowing far away from the location where the swell waves are observed. These waves can cross oceans before they reach land [51], and as they propagate, the dissipation of energy for shorter and steeper waves are more significant [5].

When the waves travel from deep to shallower water, the waves start to transform due to interaction with the seabed and land. Currents can also transform waves but is not emphasized in the following. Refraction, shoaling, and depth-induced wave breaking are caused by variations in water depth, while obstacles and slits induce diffraction and reflection.

As waves propagate towards shallower water, the wave speed decreases due to wave-seabed interaction. Since the wave energy needs to be conserved, and the wave period is constant, the wave height increases to preserve the constant energy flux, which is named *shoaling*. When the wave becomes too steep, the wave breaks, which is called *depth-induced breaking* or *shallow-water breaking*. If the wave crests approach the contours of the bathymetry at an angle, it will result in a difference in wave speed along the wave crest. The parts of the wave crest that are in shallower water will move slower, and the wave will turn towards the shallower areas. This process is called *refraction*.

The *diffraction* of water waves is the effect of waves propagating into the shadow zone behind an obstacle at another angle than the original wave direction. This process occurs due to variations in amplitude along the wave crest. Energy from higher parts of the wave crest is transferred to the smaller parts. Figure 2.1 illustrates an idealized scenario where the other physical processes are neglected. If diffraction did not exist, there would be no waves in the shadow area, and the waves would unaffectedly propagate straight towards the shoreline.

Reflection of waves is especially important for harbors and areas with a steep coastline, which can reflect the wave energy on impact. For beach-like coasts, it is often assumed that the reflected energy is neglectable. A full reflection of the wave may cause a standing wave pattern, which is especially relevant for harbor modeling.

These physical processes are further explained in [30].

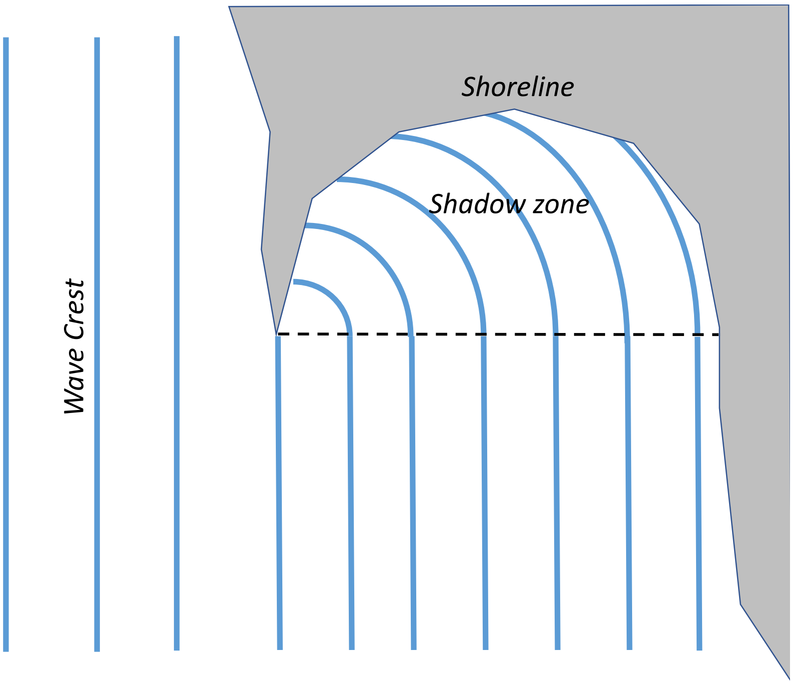

Figure 2.1: Illustration of the diffraction of water waves. Refraction and reflection are neglected.

Chapter 3

Numerical Model

This chapter presents the numerical solutions implemented in the wave model REEF3D::FNPF, as well as how the calculations are solved. This three-dimensional, fully nonlinear potential flow model is used in this study to simulate wave propagation. A fully nonlinear potential flow model is regarded as a computational efficient wave model compared to more complex CFD software. However, FNPF models do not take viscosity and turbulence into account.

3.1 Governing Equation

The Laplace equation is the governing equation for the flow calculations in the open-source fully nonlinear potential flow model REEF3D::FNPF:

$$\frac{\partial^2 \Phi}{\partial x^2} + \frac{\partial^2 \Phi}{\partial y^2} + \frac{\partial^2 \Phi}{\partial z^2} = 0 \tag{3.1}$$

where $\frac{\partial \Phi}{\partial x_i} = u_i$, Φ is the velocity potential, and u_i is the flow velocity in a spatial direction.

The Laplace equation fulfills the assumptions of the theory of potential flow:

- *Inviscid.* The flow of water could be divided into the potential flow and the boundary layer. The latter occurs around obstacles and other discontinuities where the shear forces in the flow are particularly influential. Otherwise, the flow is assumed to be inviscid, meaning that the shear stresses are neglected.

- *Incompressible.* The continuity equation (Eq. (3.2)) is fulfilled, which implies that the flow is incompressible.

$$\frac{\partial u_i}{\partial x_i} = 0 \tag{3.2}$$

- *Irrotational.* A consequence of the neglected shear forces in the water is that the flow is also assumed to be irrotational:

$$\frac{\partial u}{\partial z} + \frac{\partial w}{\partial x} = 0 \tag{3.3}$$

These three assumptions are also valid for linear wave theory since both theories are based on potential flow theory.

3.1.1 Boundary Conditions

Boundary conditions are required to solve the Laplace equation. First, the fluid particles at the free surface need to remain at the free surface, yielding the kinematic boundary condition expressed in Eq. (3.4). Another principle is that the pressure in the fluid at the free surface is equal to the atmospheric pressure, which results in the dynamic boundary condition presented in Eq. (3.5). These two principles result in the *free surface boundary conditions*:

$$\begin{aligned}\frac{\partial \eta}{\partial t} =& -\frac{\partial \eta}{\partial x}\frac{\partial \widetilde{\Phi}}{\partial x} - \frac{\partial \eta}{\partial y}\frac{\partial \widetilde{\Phi}}{\partial y} \\ & + \widetilde{w}\left(1 + \left(\frac{\partial \eta}{\partial x}\right)^2 + \left(\frac{\partial \eta}{\partial y}\right)^2\right),\end{aligned} \tag{3.4}$$

$$\begin{aligned}\frac{\partial \widetilde{\Phi}}{\partial t} =& -\frac{1}{2}\left(\left(\frac{\partial \widetilde{\Phi}}{\partial x}\right)^2 + \left(\frac{\partial \widetilde{\Phi}}{\partial y}\right)^2\right) \\ & + \frac{1}{2}\widetilde{w}^2\left(1 + \left(\frac{\partial \eta}{\partial x}\right)^2 + \left(\frac{\partial \eta}{\partial y}\right)^2\right) - g\eta.\end{aligned} \tag{3.5}$$

Where $\widetilde{\Phi} = \Phi(\mathbf{x}, \eta, t)$ is the velocity potential at the free surface, $\mathbf{x} = (x, y)$ represents the horizontal location, $\widetilde{w}$ is the vertical velocity at the free surface, and g is gravitational constant.

At the bottom, the vertical water velocity must be zero since the particles cannot penetrate the seabed. This yields the *bottom boundary condition*:

$$\frac{\partial \Phi}{\partial z}+\frac{\partial h}{\partial x}\frac{\partial \Phi}{\partial x}+\frac{\partial h}{\partial y}\frac{\partial \Phi}{\partial y}=0, \quad z=-d. \tag{3.6}$$

where $d = d(\mathbf{x})$ is the water depth from the seabed to the still water level.

3.1.2 Sigma Grid

With the implementation of the σ-coordinate scheme, the vertical grid size in the numerical model is dependent on the bathymetry. The flexible σ-coordinate system is visualized in figure 3.1, and the following equation defines the transfer function from a Cartesian coordinate system to the σ-domain:

$$\sigma=\frac{z+d\left(\mathbf{x}\right)}{\eta(\mathbf{x},t)+d(\mathbf{x})} \tag{3.7}$$

Once the velocity potential Φ is obtained in the σ-domain, the velocities can be calculated as follows:

$$u\left(\mathbf{x},z\right)=\frac{\partial \Phi\left(\mathbf{x},z\right)}{\partial x}=\frac{\partial \Phi\left(\mathbf{x},\sigma\right)}{\partial x}+\frac{\partial \sigma}{\partial x}\frac{\partial \Phi\left(\mathbf{x},\sigma\right)}{\partial \sigma}, \tag{3.8}$$

$$v\left(\mathbf{x},z\right)=\frac{\partial \Phi\left(\mathbf{x},z\right)}{\partial y}=\frac{\partial \Phi\left(\mathbf{x},\sigma\right)}{\partial y}+\frac{\partial \sigma}{\partial y}\frac{\partial \Phi\left(\mathbf{x},\sigma\right)}{\partial \sigma}, \tag{3.9}$$

$$w\left(\mathbf{x},z\right)=\frac{\partial \sigma}{\partial z}\frac{\partial \Phi\left(\mathbf{x},\sigma\right)}{\partial \sigma}. \tag{3.10}$$

3.2 Numerical Treatment of Governing Equations

The governing equations have to be discretized to solve a fluid dynamic problem numerically, both in the spatial domain and the time domain. In the spatial domain, the domain is divided into points that form cells, typically shaped as cuboids, cubes, or tetrahedrons for a three-dimensional case. Cell points are located at the corners of the cells, and this set of points is referred to as the grid or the mesh. A structured grid is a set of cells with some regularity. This decomposition is less computationally demanding than an unstructured grid. A structured grid is incorporated in REEF3D.

In REEF3D, staggered grids are used in the numerical discretization of the equations, meaning that the variables are not located at the same parts of the cell. For instance, the pressure is determined at the center of the cells, while the velocity is calculated at

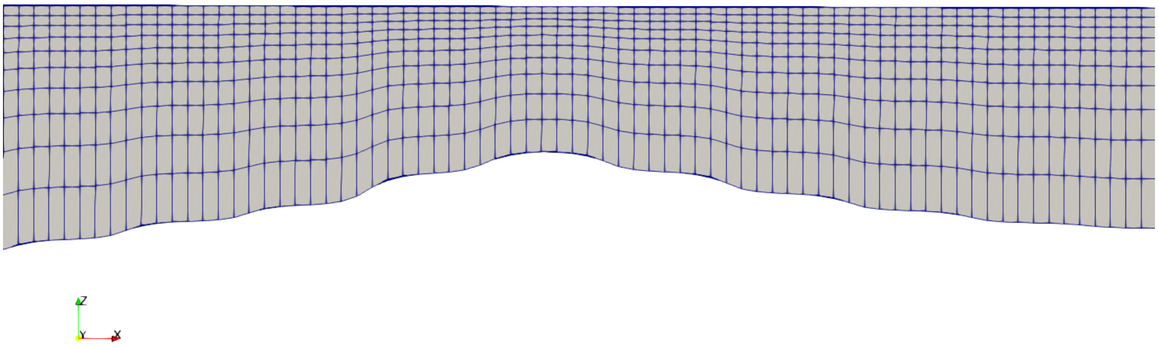

Figure 3.1: Illustration of the sigma grid over varying bathymetry.

the midpoint of the cell edges. Contrary to the other scheme referred to as collocated grids, where all the variables are located at the cell edges. This type of scheme is commonly used for unstructured grids. An advantage of using the staggered grid is that it prevents pressure oscillations [36].

Accuracy and stability are the two main aspects when evaluating numerical schemes. The error between the numerical solution and the exact solution is called the truncation error. The order of this error determines the accuracy of a numerical scheme. The numerical scheme is deemed stable if there is an upper and lower limit on the errors.

3.2.1 Spatial Discretization

With the domain decomposed into points, the governing equation also needs to be discretized by implementing numerical schemes. Spatial schemes vary in accuracy and efficiency. A numerical scheme involving more steps are generally more accurate, but also the most computationally demanding. The central difference scheme (CDS) is an example of a simple and efficient numerical scheme, while the fifth-order WENO (weighted essentially non-oscillatory) scheme [33] represents a more accurate, but also more computationally demanding spatial scheme. The WENO scheme is chosen for the discretization of the kinematic (Eq. (3.4)) and the dynamic boundary condition (Eq. (3.5)). The less expensive central difference scheme is utilized for the discretization of the Laplace equation (Eq. (3.1)).

Central Difference Scheme (CDS)

This central difference scheme makes use of the adjacent values at each side, and the error is of second-order in Δx.

$$\frac{\partial U_i}{\partial x} = \frac{U_{i+1} - U_{i-1}}{2\Delta x} \tag{3.11}$$

Weighted Essentially Non-Oscillatory (WENO) Scheme

The more expensive WENO scheme takes local smoothness into account, which makes it possible to calculate large gradients. Three local ENO-stencils are involved for a single WENO discretization. These ENO-stencils are weighted according to their smoothness, where the smoothest stencil has the most substantial contribution. The implementation of a fifth-order WENO scheme [32] for the level-set function (Eq. (3.12)) is illustrated in the following equations.

$$\phi_x = \begin{cases} \phi_x^- & if\ U_1 > 0 \\ \phi_x^+ & if\ U_1 < 0 \\ 0 & if\ U_1 = 0 \end{cases} \tag{3.12}$$

The WENO approximation for $\phi_x^\pm$ is a convex combination of the three possible ENO approximations:

$$\phi_x^\pm = \omega_1^\pm \phi_x^{1\pm} + \omega_2^\pm \phi_x^{2\pm} + \omega_3^\pm \phi_x^{3\pm} \tag{3.13}$$

The three ENO stencils defined for ϕ are

$$\begin{aligned} \phi_x^{1\pm} &= \frac{q_1^\pm}{3} - \frac{7q_2^\pm}{6} + \frac{11q_3^\pm}{6} \\ \phi_x^{2\pm} &= -\frac{q_2^\pm}{6} + \frac{5q_3^\pm}{6} + \frac{q_4^\pm}{3} \\ \phi_x^{3\pm} &= \frac{q_3^\pm}{3} + \frac{5q_4^\pm}{6} - \frac{q_5^\pm}{6} \end{aligned} \tag{3.14}$$

where,

$$\begin{aligned} q_1^- &= \frac{\phi_{i-2} - \phi_{i-3}}{\Delta x},\ q_2^- = \frac{\phi_{i-1} - \phi_{i-2}}{\Delta x},\ q_3^- = \frac{\phi_i - \phi_{i-1}}{\Delta x}, \\ q_4^- &= \frac{\phi_{i+1} - \phi_i}{\Delta x},\ q_5^- = \frac{\phi_{i+2} - \phi_{i+1}}{\Delta x} \end{aligned} \tag{3.15}$$

and

$$\begin{aligned} q_1^+ &= \frac{\phi_{i+3}-\phi_{i+2}}{\Delta x},\ q_2^+ = \frac{\phi_{i+2}-\phi_{i+1}}{\Delta x},\ q_3^+ = \frac{\phi_{i+1}-\phi_{i}}{\Delta x}, \\ q_4^+ &= \frac{\phi_{i}-\phi_{i-1}}{\Delta x},\ q_5^+ = \frac{\phi_{i-1}-\phi_{i-2}}{\Delta x} \end{aligned} \tag{3.16}$$

the weights are written as:

$$\omega_1^\pm = \frac{\alpha_1^\pm}{\alpha_1^\pm+\alpha_2^\pm+\alpha_3^\pm},\quad \omega_2^\pm = \frac{\alpha_2^\pm}{\alpha_1^\pm+\alpha_2^\pm+\alpha_3^\pm},\quad \omega_3^\pm = \frac{\alpha_3^\pm}{\alpha_1^\pm+\alpha_2^\pm+\alpha_3^\pm}, \tag{3.17}$$

and

$$\alpha_1^\pm = \frac{1}{10}\frac{1}{\left(\tilde{\epsilon}+IS_1^\pm\right)^2},\quad \alpha_2^\pm = \frac{6}{10}\frac{1}{\left(\tilde{\epsilon}+IS_2^\pm\right)^2},\quad \alpha_3^\pm = \frac{3}{10}\frac{1}{\left(\tilde{\epsilon}+IS_3^\pm\right)^2} \tag{3.18}$$

with the regularization parameter $\tilde{\epsilon} = 10^{-6}$ in order to avoid division by zero, and the following smoothness indicators:

$$\begin{aligned} IS_1^\pm &= \frac{13}{12}\left(q_1-2q_2+q_3\right)^2 + \frac{1}{4}\left(q_1-4q_2+3q_3\right)^2, \\ IS_2^\pm &= \frac{13}{12}\left(q_2-2q_3+q_4\right)^2 + \frac{1}{4}\left(q_2-q_4\right)^2, \\ IS_3^\pm &= \frac{13}{12}\left(q_3-2q_4+q_5\right)^2 + \frac{1}{4}\left(3q_3-4q_4+q_5\right)^2 \end{aligned} \tag{3.19}$$

This weighting ensures that the smoothest stencil of the three in Eq. (3.14) will have the greatest contribution.

3.2.2 Time Discretization

The time discretization is essential to ensure stability in the calculation, especially for the rapidly changing parameters found in fluid dynamics. The TVD Runge-Kutta scheme is implemented in REEF3D for this purpose.

Total Variance Diminishing (TVD) Runge-Kutta Scheme

A total variance diminishing Runge-Kutta scheme is an explicit numerical scheme developed by Harten [29], which is often used in computational fluid dynamics. The ability to capture quick changes accurately, even for relatively coarse grids, is one advantage of the TVD Runge-Kutta scheme. The third-order TVD Runge-Kutta is presented in the following.

$$
\begin{aligned}
\phi^{(1)} &= \phi^{n} + \Delta t L\left(\phi^{n}\right) \\
\phi^{(2)} &= \frac{3}{4}\phi^{n} + \frac{1}{4}\phi^{(1)} + \frac{1}{4}\Delta t L\left(\phi^{(1)}\right) \\
\phi^{n+1} &= \frac{1}{3}\phi^{n} + \frac{2}{3}\phi^{(2)} + \frac{2}{3}\Delta t L\left(\phi^{(2)}\right)
\end{aligned}
\tag{3.20}
$$

The term ‘L’ represents the spatial discretization. For the time treatment in this study, a third-order accurate TVD Runge-Kutta scheme [53] is used.

3.2.3 Adaptive Time-Stepping

The method of adaptive time-stepping is implemented, which adjust the time step based on the grid size, maximum particle velocity, and the maximum depth. A constant time factor, equivalent to the CFL condition, is introduced. The time steps are determined as follows:

$$
\begin{aligned}
&c_u = \frac{\Delta x}{\left|max(u_{max}, 1.0\sqrt{9.81 * h_{max}})\right|}, \\
&c_v = \frac{\Delta x}{\left|max(v_{max}, 1.0\sqrt{9.81 * h_{max}})\right|}, \\
&c_{tot} = min(c_u, c_v), \\
&\Delta t = c_{tot} CFL.
\end{aligned}
\tag{3.21}
$$

Where u_{max}, v_{max} are the maximum particle velocities in x and y directions, and h_{max} is the maximum water depth.

3.3 Wave Generation and Absorption

For a basic configuration, the numerical wave tank consists of a zone where the waves are generated based on different theories implemented in the software. Numerous wave theories that can be imposed at this boundary are available in REEF3D. Additionally, there exists a numerical beach where the wave energy is dissipated, reducing the particle velocity to zero, and the pressure to hydrostatic conditions. The propagation of waves occurs in the working zone, between the wave generation zone and the wave absorption zone. This simple configuration is illustrated in figure 3.2. However, more complicated arrangements are possible, like a three-dimensional domain with generation and absorption zones only covering parts of the boundary.

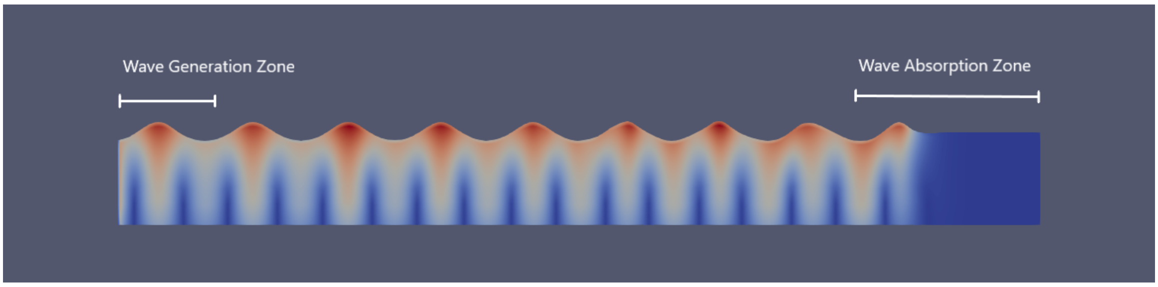

Figure 3.2: Illustration of a 2D wave tank with wave generation zone and wave absorption zone.

3.3.1 Relaxation Method

Several numerical approaches can be implemented at the wave generation zone to impose the waves, and at the numerical beach to dissipate the energy — one of those being the relaxation method [40]. In this model, the relaxation function proposed by Jacobsen [31] is used. In the wave generation zone, the theoretical values for particle velocity and pressure are imposed over the distance of the generation zone. Contrary to the wave absorption zone, where the particle velocity is reduced to zero, and pressure decreased to hydrostatic conditions following Eq. (3.22) and Eq. (3.23).

$$\begin{aligned} u_{relaxed} &= \Gamma(x)u_{analytical} + (1-\Gamma(x))u_{computational} \\ p_{relaxed} &= \Gamma(x)p_{analytical} + (1-\Gamma(x))p_{computational} \end{aligned} \tag{3.22}$$

$$\Gamma(\widetilde{x}) = 1 - \frac{e^{(\widetilde{x}^{3.5})} - 1}{e-1} \; for \; \widetilde{x} \in [0;1] \tag{3.23}$$

where $\widetilde{x}$ is scaled to the length of the relaxation zone.

3.4 Wave Breaking

A combination of how the governing equations are solved and the fact that turbulence and viscosity are neglected makes it impossible for the FNPF wave model to explicitly simulate the overturning crest and the turbulence following the collapse. Empirical-based formulations are therefore introduced in the numerical model to account for both deep-water breaking and depth-induced breaking. Breaking is identified if the steepness of the wave exceeds a specific value β, or the vertical particle velocity exceeds a fraction α of the shallow water celerity. After the breaking wave is detected,

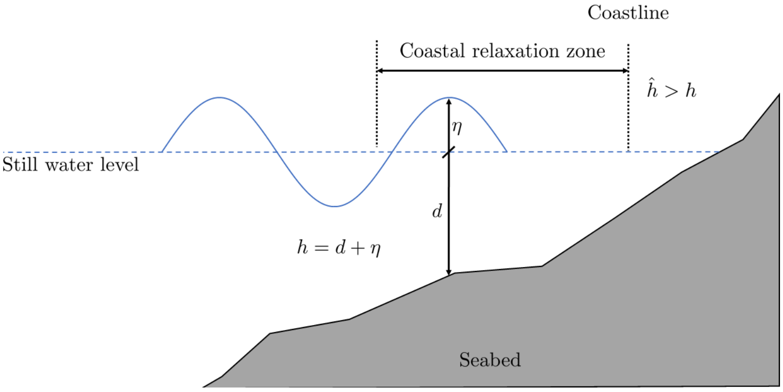

Figure 3.3: Illustration of the numerical coastal zone.

wave energy is dissipated locally by introducing a viscous damping term in the free surface boundary conditions in the area where the breaking is detected [6].

In deep water, the wave breaking criterion associated with wave steepness is used:

$$\frac{\partial \eta}{\partial x} \geq \beta \tag{3.24}$$

In shallow water domain, the depth-induced wave breaking is detected following this criterion:

$$\frac{\partial \eta}{\partial t} \geq \alpha \sqrt{gd}. \tag{3.25}$$

In this study, the input parameters α and β are set to 0.6 [20] and 1.25, respectively.

3.5 Coastline Damping

In addition to the wave breaking algorithm and the wave absorption zone along the edges of the domain, there is a third way that energy is dissipated in the model: the coastline damping zone. The interaction between the moving water and the land could cause problems for numerical solvers if not treated with caution. One source of instability is due to very shallow water, which occurs close to the coastline. As the depth approaches infinitesimally small, a divergence of the depth-dependent calculations is possible. Another challenge is to determine what is water and what is defined as land.

In REEF3D, a threshold water depth $\hat{h}$ is used to determine which cells that are to be considered as dry cell, and which that are wet. If a cell is defined as dry, the velocity is set to zero. The water depth h is defined as the sum of the still water level d and the surface elevation η (see figure 3.3).

$$\begin{cases} u = 0, & if\ h < \hat{h} \\ v = 0, & if\ h < \hat{h} \end{cases} \tag{3.26}$$

After the cells are sorted in dry and wet cells, a level-set function [46] is used to identify the shoreline, denoted Γ:

$$\phi(\vec{x}, t) = \begin{cases} > 0 & if\ \vec{x} \in\ wet\ cell \\ = 0 & if\ \vec{x} \in\ \Gamma \\ < 0 & if\ \vec{x} \in\ dry\ cell \end{cases} \tag{3.27}$$

A level-set method is also used to determine the distance perpendicular to the coastline. The distance between a certain point and the coastline is determined by the signed distance property incorporated with the level-set method. However, these values need to be updated for every iteration to ensure mass conservation as the exact shoreline evolves. A partial differential equation-based reinitialization procedure presented by Sussmann et al. [54] is implemented to update the values.

$$\frac{\partial \phi}{\partial \tau} + S(\phi)\left(\left|\frac{\partial \phi}{\partial x_j}\right| - 1\right) = 0 \tag{3.28}$$

where S(ϕ) is the smooth signed function by [47].

$$S(\phi) = \frac{\phi}{\sqrt{\phi^2 + \left|\frac{\partial \phi}{\partial x_j}\right|^2 (\Delta x)^2}} \tag{3.29}$$

The signed distance property is restored by solving Eq. (3.28) until equilibrium is achieved. The sign function in Eq. (3.29) assigns the value of zero to the coastline, and according to Eq. (3.27) for the rest of the domain.

As illustrated in figure 3.3, another measure to prevent numerical instabilities is to implement relaxation zones on the wet side of the coastline. A consequence is that modeling of run-up is not conducted. However, for many cases, this is not of interest.

3.6 Parallel Processing

In the field of computational fluid dynamics, one frequently ends up with domains that are decomposed into millions of cells. The workload is therefore distributed across multiple processors to handle this immense number of calculations. In REEF3D, the parallelized geometric multi-grid algorithm, provided by hypre [26], solves the Laplace equation. hypre is a software library of high-performance preconditioners and solvers. This library is used to solve large, sparse linear systems of equations on parallel processors and is one of the most time-consuming processes in numerical modeling of fluids. The efficiency of the solvers in this library depends on the type of grid. REEF3D uses a structured grid with a sigma grid in the vertical direction, which opens the possibility to use the most efficient solvers of this library [25]. One of those being the BiCGStab algorithm, developed by van der Vorst [55] and applied in REEF3D.

Every processor is assigned with a subdomain. In these subdomains, the neighboring points determine the value at a specific grid point. For calculations at the edge of these subdomains, ghost cells are introduced to ensure communication between adjacent points that are allocated to different processors. These ghost cells are updated with the values from the neighboring processors via MPI (Message Passing Interface) [38].

Chapter 4

Determination of Sea States

Bjørnafjorden is a perfect example of the challenges Norwegian fjords causes numerical wave models with the rapidly varying and irregular bathymetry, and are therefore used in this study to test the capability of REEF3D::FNPF. For a wave to propagate from an offshore location to Bjørnafjorden, it needs to pass either Selbjørnsfjorden and Langenuen in the south or Korsfjorden and partly Lysefjorden in the north. In the following, these two pathways will be referred to as the southern channel and the northern channel.

Figure 4.1: Bjørnfjorden, the northern channel (Korsfjorden), and the southern channel (Selbjørnsfjorden). *Screenshot from UT.no.*

There are several ways to determine the properties of the incident waves at an off-

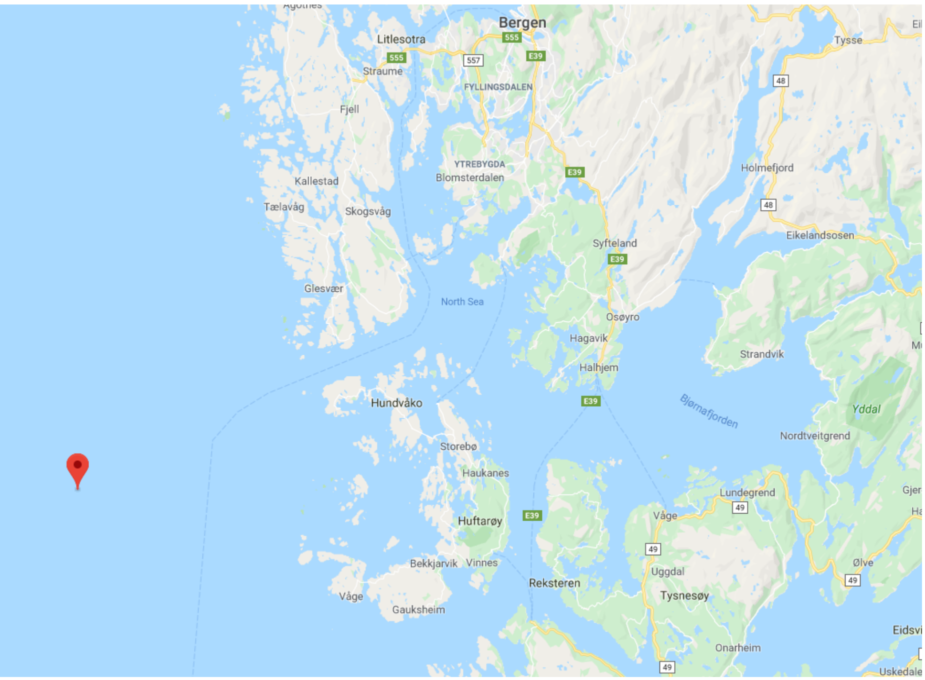

Figure 4.2: Location of the NORA10 data. Coordinates: 60.0600 N, 4.6900 E. *Screenshot from Google Maps.*

shore location. The following sections present two different approaches: based on measurements (Section 4.1), and based on NORSOK standards. This information results in five separate wave inputs that are simulated in the domain.

The majority of the procedures and the argumentation used to develop reasonable wave inputs in Section 4.1 and Section 4.2 are replicated from an earlier submitted project report [18].

4.1 NORA10

During the last 61 years, waves and wind measurements west of Bjørnafjorden (see figure 4.2) have been recorded and gathered in the NORA10 datasets. These datasets are used to get an estimate of realistic wave inputs for the numerical simulations in this thesis.

The directional distribution of the wave energy is presented with the help of wave roses in figure 4.3, figure 4.4, and figure 4.5. The eastern direction is the dominant wave direction, especially when considering the swell waves. For wind-waves, the dominant wave direction are propagation in a northern direction.

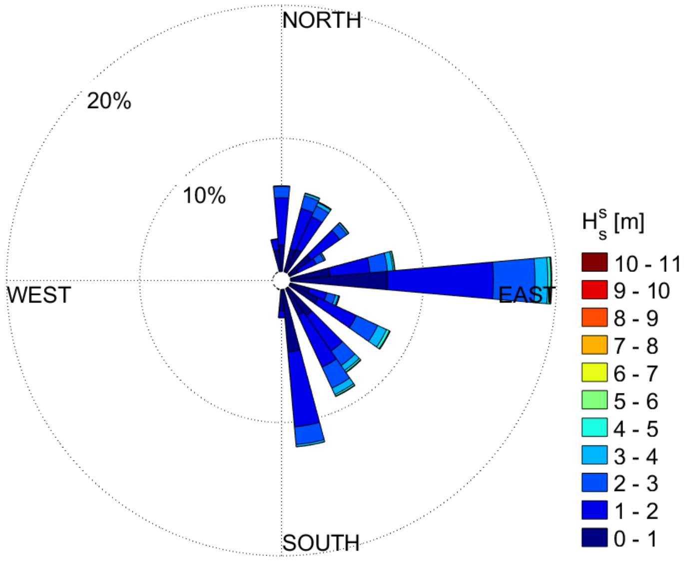

Figure 4.3: Wave rose for swell waves at NORA10.

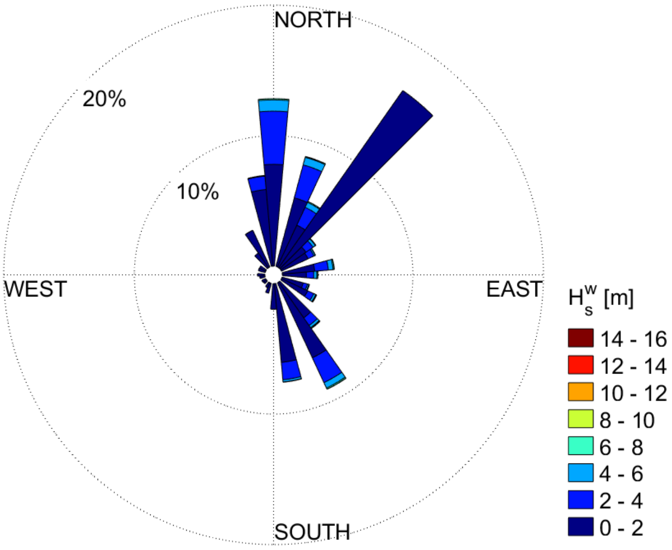

Figure 4.4: Wave rose for wind waves at NORA10.

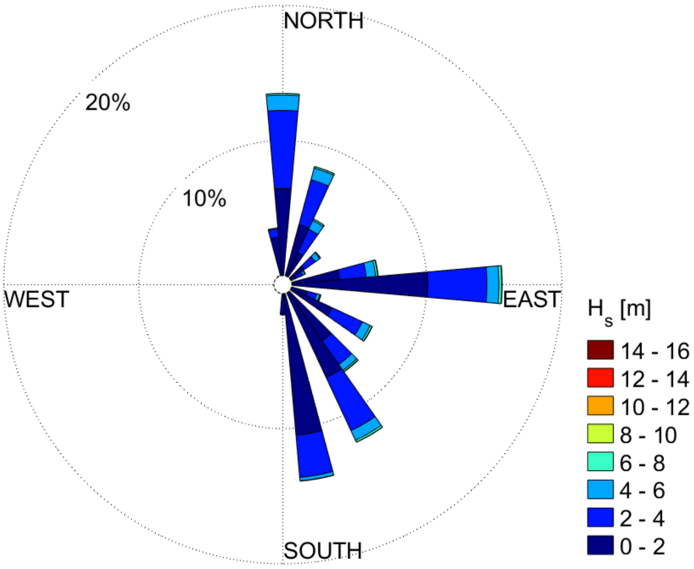

Figure 4.5: Wave rose at NORA10.

The waves of smaller amplitudes are of minor concern in this analysis. Therefore, the data presented in figure 4.5 has been filtered so that only waves with a significant wave height above eight meters are included. These results are illustrated in figure 4.6, which shows that the biggest waves are propagating in eastern and southeastern direction. It also leads to the conclusion that the smaller waves are dominant in the southern and northern directions. Based on these results, the direction of the incoming waves in the simulation is chosen to be 0, 45, and 315 degrees, where 0 zero degrees is equal to propagation towards the east in REEF3D.

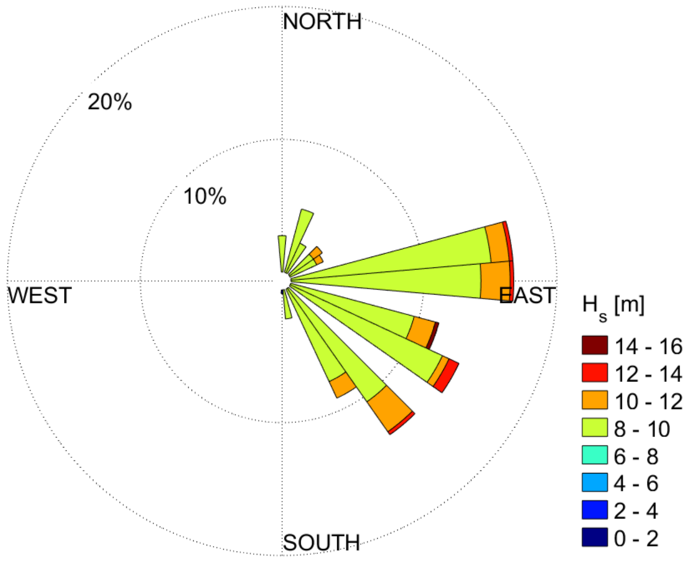

Figure 4.6: Wave rose at NORA10 for measurements with a wave height larger than eight meters.

In the numerical simulations of Bjørnafjorden, different wave heights and wave periods are used as input. One of the simulations is completed with incident wave heights equal to the maximum recorded wave height at NORA10 ($H_s = 14.2\,m$), and its corresponding wave period ($T_p = 14.9\,s$).

4.2 Wave Inputs

The following incident waves are imposed at the western boundary and simulated in the domain. H_s is the significant wave height, and T_p is the peak period.

- **Wave Input 1 (WI1):** $H_s = 15.0\,m$, $T_p = 16.0\,s$. These wave properties are taken from the NORSOK STANDARD N-003 [44]. The significant wave height (H_s) and the related maximum peak period (T_p) for a 100-year return period and a 3 hours sea state on the Norwegian coast are found in figure 1 of the standard. These input wave properties is used in three of the simulations, with the main wave directions found in Section 4.1:
  - 0 degrees: waves propagating towards the east.
  - 45 degrees: waves propagating towards the northeast.
  - 315 degrees waves propagating towards the southeast.
- **Wave Input 2 (WI2):** $H_s = 14.2\,m$, $T_p = 14.9\,s$. The largest significant wave height in the NORA10-dataset is used with the corresponding peak period. See

Section 4.1. The simulation is performed with a main incident wave direction of 0 degrees.

- **Wave Input 3 (WI3):** $H_s = 18.0\,m$, $T_p = 21.8\,s$. 21.8 seconds is the largest recorded peak period in the NORA10-dataset, while the significant wave height is just a random big wave. The simulation is performed with a main incident wave direction of 0 degrees.

The simulations with Wave Input 1 is emphasized in this study since it is based on the significant wave height for a return period of 100-years on an offshore location.

4.3 Determination of Input Wave Properties

Two-dimensional and three-dimensional simulations on a smaller domain are used to validate the numerical model. Regular waves are used to make the simulation more transparent and hence increase the probability of detecting deviations. REEF3D offers a variety of different wave theories for the incident waves, so calculations are needed to determine the correct wave theory for all three wave inputs.

4.3.1 Wavelength at the Wave Generation Zone

The linear wave dispersion relation is at first assumed to be valid, which holds only if the correct wave theory shows to be either linear wave theory or second-order Stokes waves. Recall from Section 2.2 that the dispersion relation for second-order Stokes waves is equal to the one for linear wave theory.

There are several methods to solve the dispersion relation for arbitrary depth, depending on the mathematical numerical method used [58]. One common method is Bob You's approximation formula:

$$L_0 = 1.56T^2 \qquad\qquad k_0 = \frac{2\pi}{L_0} \tag{4.1}$$

$$\xi_0 = \sqrt{k_0\,d}\,(1 + \frac{k_0\,d}{6} + \frac{(k_0\,d)^2}{30}) \tag{4.2}$$

$$L = L_0\,tanh(\xi_0) \tag{4.3}$$

Where L is the wavelength, T is the wave period, k is the wavenumber, and d is the depth. The subscript '0' indicates a deep water parameter. The shallowest part of the numerical wave generation zone ($d = 170m$) is used in the calculation because it is the conservative choice for these specific conditions. Inserting the values provided in Section 4.2 into Eq. (4.1), (4.2), and (4.3), yields the following results:

	H_s	T_p	L_0	$k_0\,d$	ξ_0	L	d/L	
Wave Input 1	$15.0\,m$	$16.0\,s$	$399.4\,m$	2.67	2.75	$396.2\,m$	0.43	Intermediate water
Wave Input 2	$14.2\,m$	$14.9\,s$	$346.3\,m$	3.08	3.21	$345.2\,m$	0.49	Intermediate water
Wave Input 3	$18.0\,m$	$21.8\,s$	$741.4\,m$	1.44	1.57	$680.0\,m$	0.25	Intermediate water

Table 4.1: Calculation of wavelength for the three wave inputs. In linear wave theory, deep water is $d/L > 0.5$, shallow water is $d/L < 0.05$, and intermediate water depth between these.

4.3.2 Applicable Wave Theory at the Wave Generation Zone

The work by Le Méhauté [37] is used to determine which wave theory that applies to these conditions. The values for Eq. (4.4) are presented in table 4.2. By inserting these dimensionless numbers into figure 4.7, it is apparent that Wave Input 1 (red), Wave Input 2 (purple), and Wave Input 3 (orange) are all in the range of second-order Stokes waves under these conditions.

$$\text{Y-axis: } \frac{H_s}{g \cdot T_p^2} \qquad \text{X-axis: } \frac{d}{g \cdot T_p^2} \tag{4.4}$$

	$\frac{H_s}{g\,T_p^2}$	$\frac{d}{g\,T_p^2}$	Applicable wave theory
Wave Input 1	0.0060	0.068	Second-order Stokes waves
Wave Input 2	0.0065	0.078	Second-order Stokes waves
Wave Input 3	0.0039	0.036	Second-order Stokes waves

Table 4.2: Dimensionless wave height and depth for figure 4.7.

The Ursell parameter is another criterion that indicates if the theory of Stokes waves applies. The theory of Stokes is considered to be applicable as long as $Ur < 10$ [30]. Wave Input 3 includes the highest and longest waves, so for Eq. (4.5), it is only necessary to check these conditions. Since $Ur < 10$ for Wave Input 3, it is also valid for the remaining wave inputs.

$$Ur = \frac{H_s L^2}{d^3} = \frac{18.0m \cdot (680.0m)^2}{(170.0m)^3} = 1.69 < 10 \tag{4.5}$$

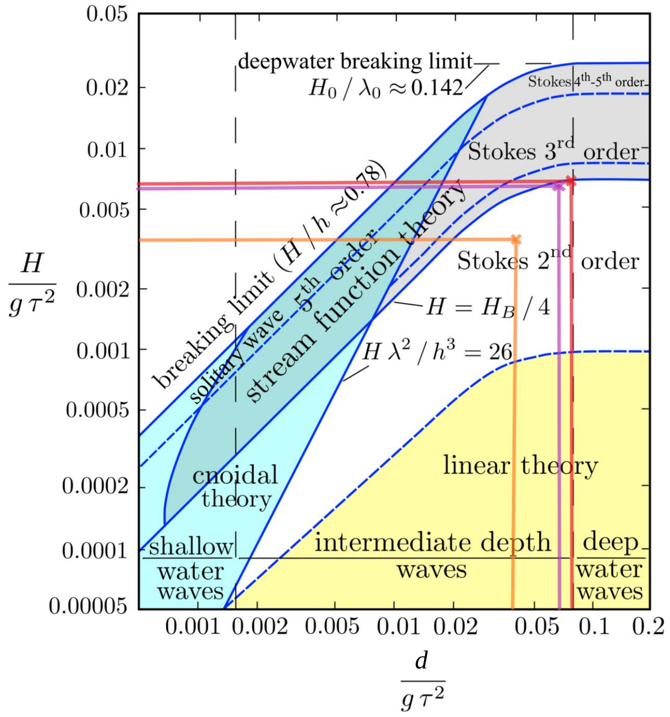

Figure 4.7: The ranges of applicability for different wave theories. The values from table 4.2 are illustrated in different colors.

Both of these theories confirm the assumption that the linear wave dispersion relation is valid for all three wave inputs, and that the applicable wave theory is the second-order Stokes waves. Consequently, the regular waves in Section 5.1 and Section 5.2 are imposed as second-order Stokes waves.

Chapter 5

Verification of the Numerical Model

In this chapter, the validity of the model is tested, and different parameters of the numerical model are justified. While Chapter 2 and Chapter 3 present several theories and numerical methods used in this study, this chapter focus on determining the parameters, like the required coastal damping distance and the numerical grid size, both vertically and horizontally.

The topography, provided by the NPRA, is implemented in a 45 km long, and 35 km wide numerical wave tank (see figure 5.1), which is discretized by a numerical grid. The five different wave inputs presented in Section 4.2 are imposed on the western boundary of the domain.

The bathymetry of this area perfectly illustrates the challenging nature of numerical wave modeling in Norwegian fjords. Numerous small islands and skerries demand an accurate numerical model, and sharp gradients in the bathymetry require a numerical scheme that can handle it. There is only 600 meters, horizontally, between the deepest spot in the domain and land. The higher-order WENO scheme is therefore used for the spatial discretization of the kinematic and dynamic boundary conditions at the free surface. In contrast, central differences of the second order are used for the discretization of the Laplace equation, while third-order TVD Runge-Kutta is the time scheme used in this study.

5.1 Grid Convergence Study

A grid convergence is used to determine the fixed mesh size in the horizontal directions. The goal is to optimize the grid size so that it will replicate the wave action

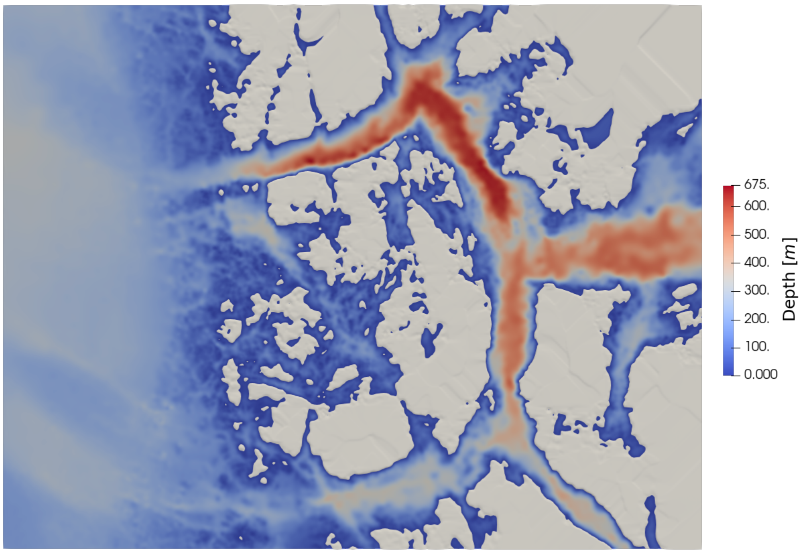

Figure 5.1: Bathymetry of the domain. *Screenshot from Paraview.*

accurately with as few cells as possible to reduce the computational cost.

One challenge is to overcome numerical diffusion. Numerical diffusion refers to artificial damping of the amplitude, as compared to the exact solution. The discretization of a continuous equation, like the Laplace equation, will result in a discrete equation that is more diffusive than the original equation. One way to reduce numerical damping is to use higher-order numerical schemes [39], like WENO, which is used in this study.

Another method to minimize numerical diffusion is grid refinement. A two-dimensional grid convergence study is conducted in this section to determine the necessary number of meshes per wavelength. Firstly, a numerical wave tank with constant depth is used. The results are then further validated with a two-dimensional wave tank with varying topography, extracted from the original domain. Wave Input 1 is imposed at the boundary, and the number of meshes in the vertical direction is fixed at ten.

For the simulations of the entire domain, a CFL factor of 1.0 is used to determine the time step. Since the maximum depth is 669 m, and the maximum particle velocity is smaller than 10 m/s, the time step is determined by the depth according to Eq. (3.21). Constant time steps for different mesh sizes are therefore used throughout the grid convergence study. Calculation of Eq. (3.21) yields the time steps presented in table 5.1.

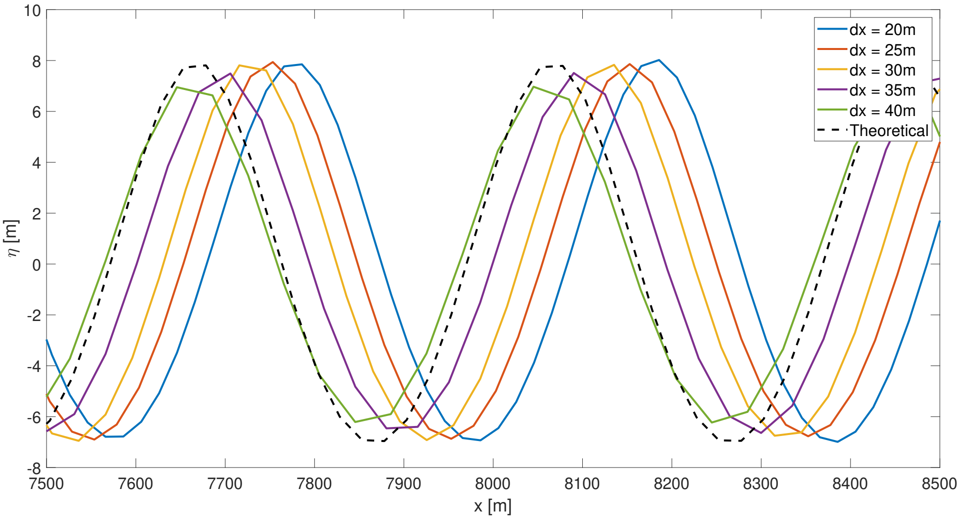

Figure 5.2: The free surface elevation for different grid sizes for a constant depth, compared to the theoretical solution.

$\Delta x[m]$	**Number of meshes per wavelength**	$\Delta t[s]$
20	20	0.247
25	16	0.309
30	13	0.372
35	11.5	0.434
40	10	0.497

Table 5.1: Number of meshes per wavelength for Wave Input 1, and the corresponding time step used in the simulations for different grid sizes.

5.1.1 Constant Depth

Since the domain covers such a vast area, even small deviations in the numerical simulation might cause significant discrepancies over such long distances. Therefore, a 10 kilometers long numerical wave tank is used in this grid convergence study. Like the calculations in Section 4.3, the depth is determined by the shallowest part of the numerical wave generation zone, which is 170 meters.

Figure 5.2 shows that numerical diffusion will occur, but is neglectable for grid size finer than 35 m. The same result is notable in table 5.2, where the error of the extremes is quantified to be approximately one percent of the theoretical solution. However, some deviations are to be expected since the discretized points might not always coincide with the extremes. Grid sizes of 20 m, 25 m, and 30 m correspond to 20, 16, and 13 meshes per wavelength, respectively. Phase-shifting or numerical dispersion is also evident, but this inaccuracy is addressed in Section 5.2.

5.1.2 Varying Depth

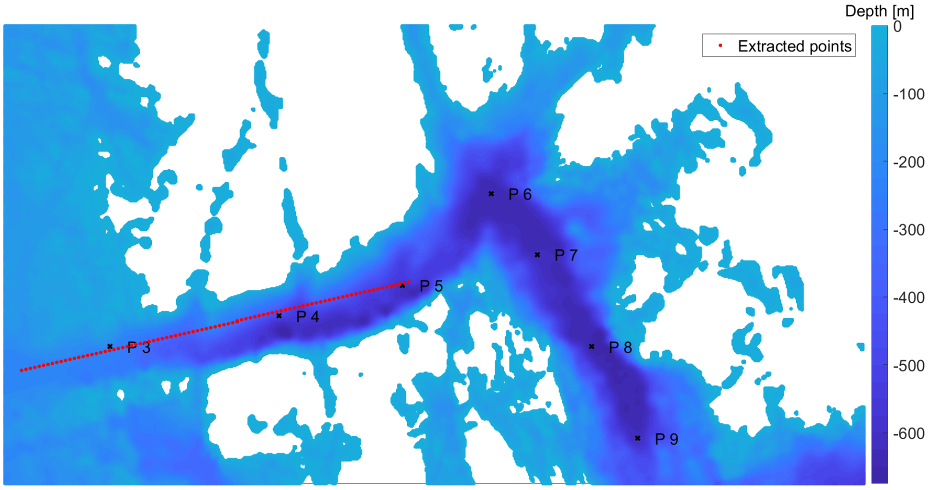

Figure 5.3: Northern channel with illustration of the extracted points used for 2D bathymetry, and the position of the wave gauges.

The two-dimensional bathymetry is extracted directly from the northern channel to make a representable bathymetry for the one-dimensional simulation. Figure 5.3 illustrates the extracted points, in addition to the numerical wave gauges located in the channel. The resulting bathymetry is presented in figure 5.4.

By including the varying bathymetry, the results will additionally indicate how well the numerical wave model handles the wave-seabed interaction — specifically, the shoaling/deshoaling process. The deshoaling process is challenging to replicate for the popular shallow water wave models. Eldrup and Andersen [24], and Beji and Battjes [7] showed that waves propagating towards deeper water decomposes into higher frequency wave components for steep slopes, which makes the shallow water assumption invalid in some cases. However, Hans Bihs et al. [11] demonstrated, through a case study, that the potential flow model REEF3D::FNPF is capable of replicating the deshoaling process accurately.

Simulations of a numerical wave tank with varying bathymetry (figure 5.5) reveal that also a grid size of 30 m is insufficient to replicate the wave action. On the other hand,

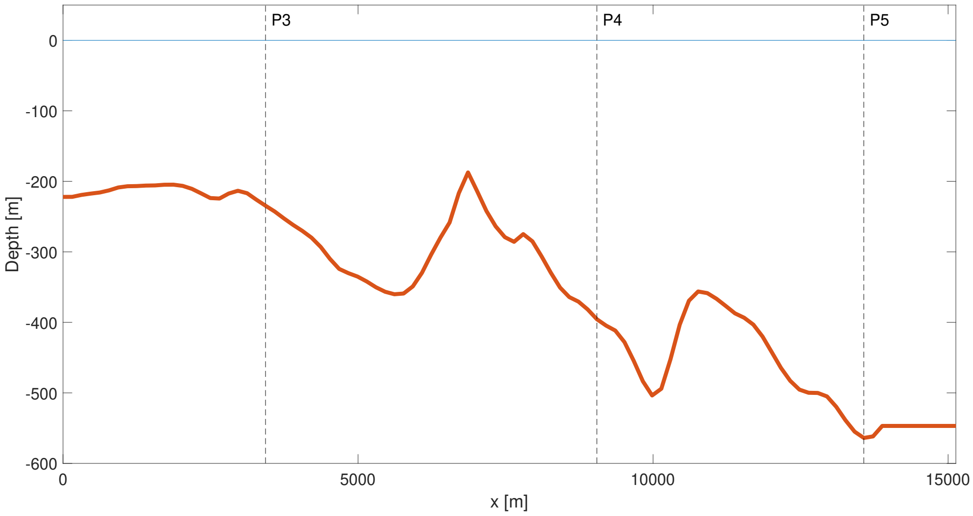

Figure 5.4: The two-dimensional topography extracted from the points in figure 5.3, and the location of the wave gauges.

.

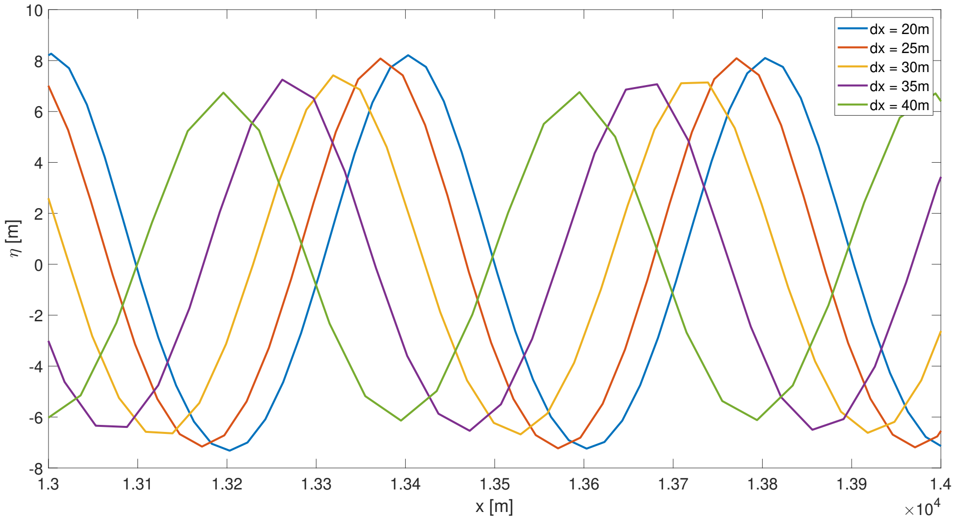

Figure 5.5: The free surface elevation of waves simulated over the bathymetry presented in figure 5.4.

	dx = 40 m	**dx = 35 m**	**dx = 30 m**	**dx = 25 m**	**dx = 20 m**
Constant depth	10.7 %	4.84 %	1.00 %	1.61 %	1.12 %
Varying depth	16.51 %	11.73 %	9.62 %	0.62 %	-

Table 5.2: Errors in numerical results for wave crests and wave troughs relative to theoretical values for constant depth (for $7500\,m \leq x \leq 8500\,m$), and relative to a simulation with dx = 20 m for varying depth (for $13000\,m \leq x \leq 14000\,m$).

a refinement of the mesh from 25 m to 20 m will not improve accuracy significantly, which is further validated by the values presented in table 5.2. The conclusion is that a mesh size of 25 meters in the horizontal directions is necessary to avoid numerical damping and to capture wave-seabed interaction accurately. Numerical dispersion is visible, but this source of error is addressed in the following section.

5.2 Vertical Stretching of the Computational Grid

While errors in magnitude are termed dissipation, errors in phase are called dispersion. Both of these physical processes occur naturally in most physical systems described by partial differential equations. For water waves, shallow water waves are non-dispersive, which implies that the phase velocity is equal to the group velocity. Deep water waves, on the contrary, are dispersive, indicating that the phase velocity is higher than the group velocity. Other physical processes, such as refraction, diffraction, and breaking, are closely related to dispersion.

Like numerical dissipation, the discretization of an equation could similarly introduce numerical dispersion, which is visible in figure 5.2 and figure 5.5. Numerical dispersion is a well-known problem related to numerical wave models and is a result of the wave model either under- or overestimating the wave speed of a wave component.

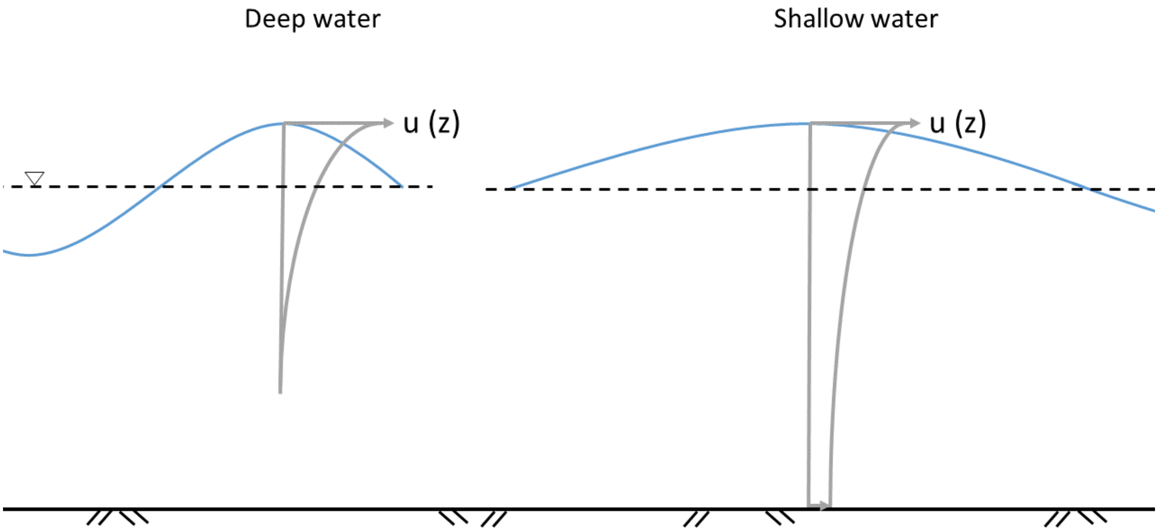

Figure 5.6: Distribution of particle velocity in the vertical direction (z-direction).

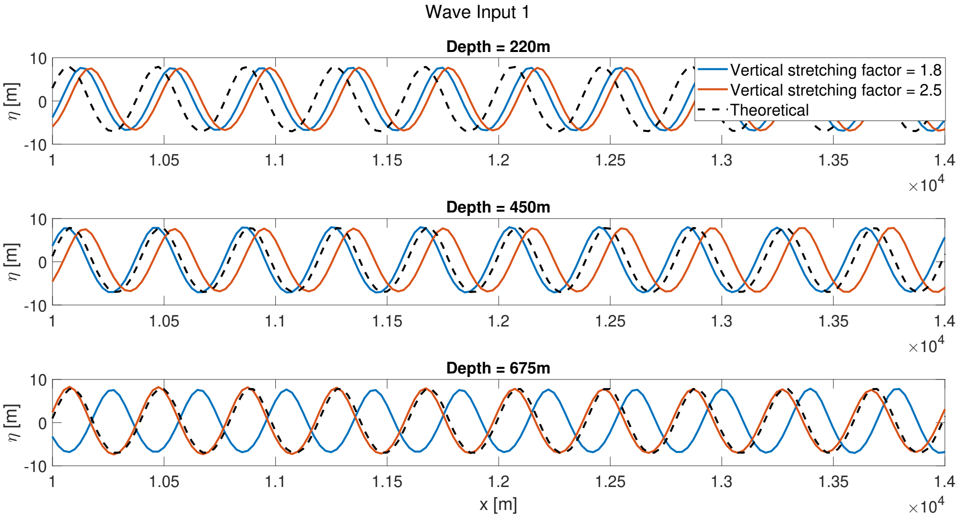

Figure 5.7: Free surface elevation, at different depths, with different vertical stretching factors for Wave Input 1.

One way to change numerical dispersion is to adjust the grid size both vertically and horizontally, but this is computationally demanding. Another way is to use a nonuniform mesh in the vertical direction. In this study, ten cells are used in the vertical direction. Grid stretching with the focus point at the free surface (see figure 3.1) is introduced to capture the velocity profile more accurately. For shallow water, a uniform mesh is reasonable since the particle velocity of the waves extends down to the seabed, as visualized in figure 5.6. However, for deeper water and a uniform mesh, the velocity profile is only captured by some of the cells closest to the surface. Consequently, adjusting the vertical stretching factor of the numerical grid in simulations for deeper water will have a more significant impact on the results than for shallower water, which is especially visible for shorter waves (see figures 5.7 and 5.8).

Since the most accurate amount of vertical stretching depends on the depth, it implies that there is no one correct answer for this domain. In other words, artificial phase-shifting will occur, but the aim is to reduce it to a neglectable amount. By investigating figure 5.1, it is evident that the depth off the coast, in the northern channel, southern channel, and Bjørnafjorden is ranging from 325 m to 675 m (except for some subsea ridges in the southern channel). To get the most accurate vertical stretching factor for these depths is therefore emphasized.

Numerous simulations with different vertical stretching factors have been conducted. In figure 5.7, 5.8, and 5.9, two of the most accurate solutions are presented. Waves in deep water require a high factor of vertical stretching to avoid significant phase-

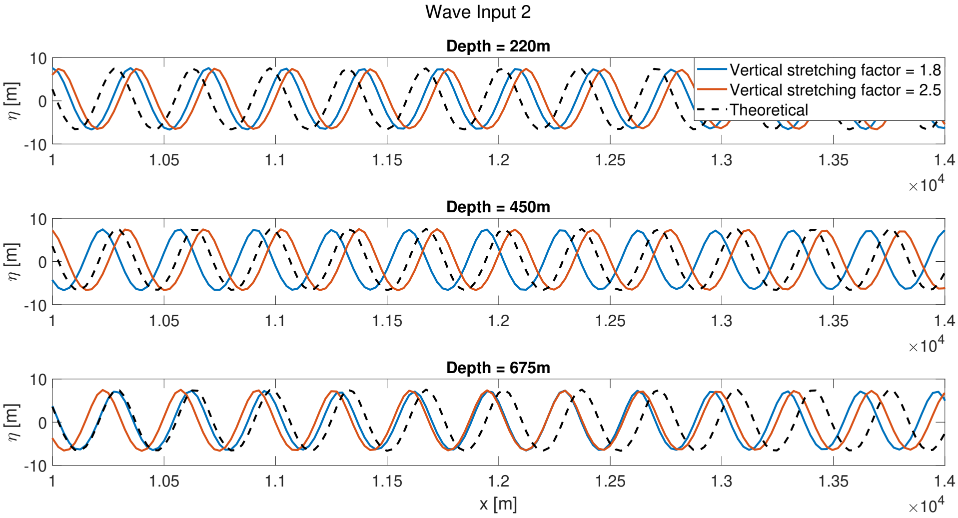

Figure 5.8: Free surface elevation, at different depths, with different vertical stretching factors for Wave Input 2.

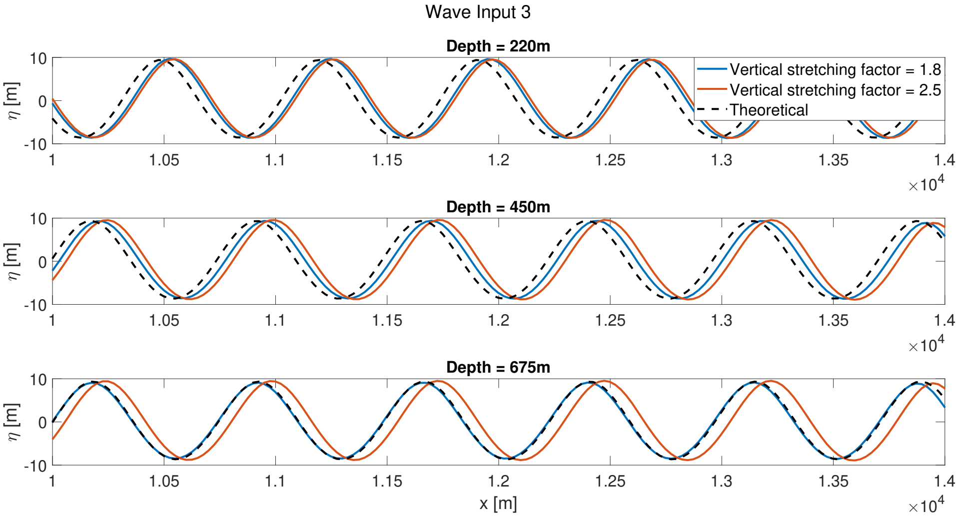

Figure 5.9: Free surface elevation, at different depths, with different vertical stretching factors for Wave Input 3.

shifting. Comparing the results for WI3 to WI1 and WI2, it is evident that a refinement of the grid close to the free surface is necessary to replicate the wave motion in deep water (wavelength small compared the to depth) accurately. For longer waves, like WI3, a vertical stretching of the grid will not influence accuracy considerably, especially compared to the effect that is visible for WI1 and WI2.

Using a vertical stretching factor of 1.8 will result in a significant lagging phase error (one wave period per 10 km) for the deepest parts of the domain for WI2. A lagging phase error means that wave speed is less than the analytical solution, the opposite of a leading phase error. For shallower depths, the result of this factor is more accurate. On the other hand, a vertical stretching factor of 2.5 results in a small lagging phase error (approximately one wave period per 100km) for a depth of 675 meters. The leading phase errors of the results from the shallower domains are in the same order of magnitude. Similar results are shown for WI1.

Unlike the one-dimensional simulations in this section, the large-scale simulations will be conducted with irregular incident waves made up of 2048 regular wave components. The wave periods of these components are determined by the JONSWAP spectrum. This implies that shorter wave components will also be generated for the simulation of WI3. With that in mind, it is reasonable to use a vertical stretching factor of 2.5 for all simulations to ensure that the wave model is able to capture the velocity profile of shorter waves in deep water, thus reducing the numerical dispersion.

5.3 Coastal Damping Distance

Section 3.5 presents the theory of how REEF3D::FNPF incorporates a numerical coastline. This method requires two inputs by the user: the threshold water depth and the coastline damping distance.

The threshold water depth $\hat{h}$ is set to 10 cm.

The coastline damping distance is the length of the coastal relaxation zone (see figure 3.3). The determination of this parameter is a trade-off between unphysical damping and reflection of the coastline. A small coastal relaxation zone may cause a reflection off the numerical shoreline because the energy of the waves is not entirely dissipated within the relaxation zone. On the other hand, a more extended coastal relaxation zone might reduce waves traveling along the coastline. In this study, the importance of diffraction is high, and a considerable damping distance will unrealistically miti-

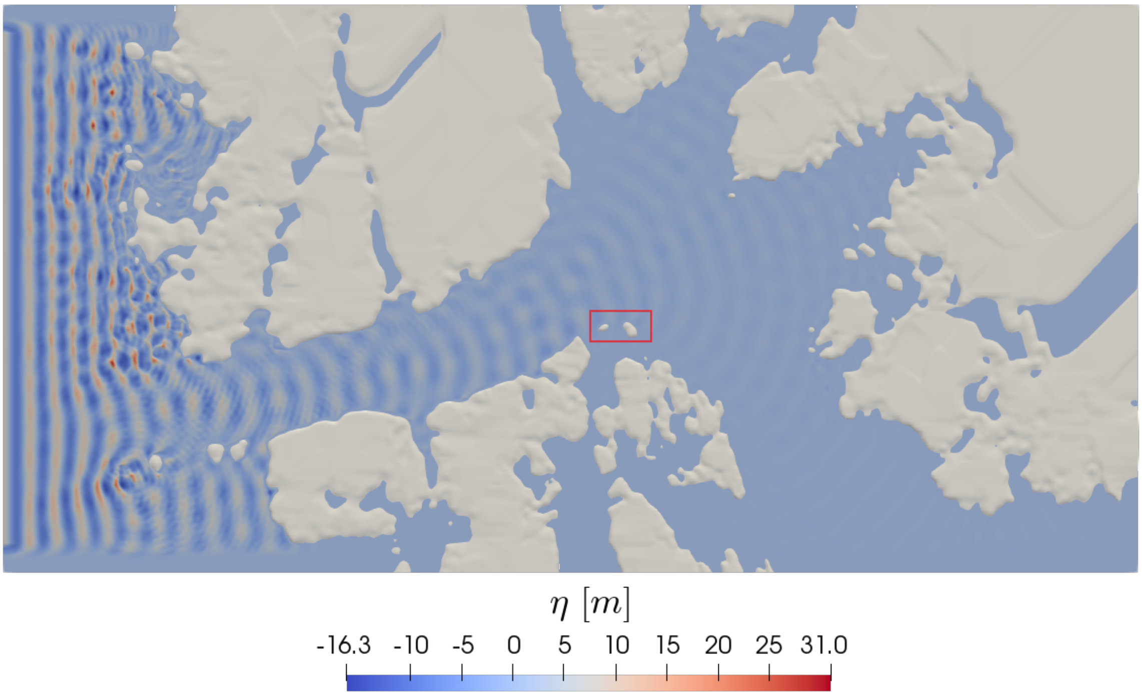

Figure 5.10: Location of Eldjarnet and Kyrholmen, highlighted by a red box.

gate the effect.

An example is the wave propagation around Eldjarnet and Kyrholmen (see figure 5.10). An extensive coastline damping distance dissipates the energy from waves traveling around these islands and towards Bjørnafjorden, and therefore reduces the fidelity of this study.

The purpose of this part of the thesis is to find the smallest damping distance that does not result in an unphysical reflection of waves. Simulations of the northern channel combined with WI3 are used to determine the required damping distance.

Figure 5.11, 5.12, and 5.13 visualize the particle velocity at the numerical coastline for a coastline damping distance of 100 m, 120 m, and 200 m, respectively. Figure 5.13 illustrates that a damping distance of 200 m substantially dissipates the energy of the waves all over the domain. However, the dissipation process is too substantial, which is visualized in figure 5.16. A damping distance of 200 m causes a dissipation of waves traveling parallel to the coastline at depths of up to 300 m, which is unrealistic.

Contrarily, a coastline damping distance of 100 m results in less unphysical damping. Figure 5.14 shows that the coastal relaxation zone extends to depths of approximately

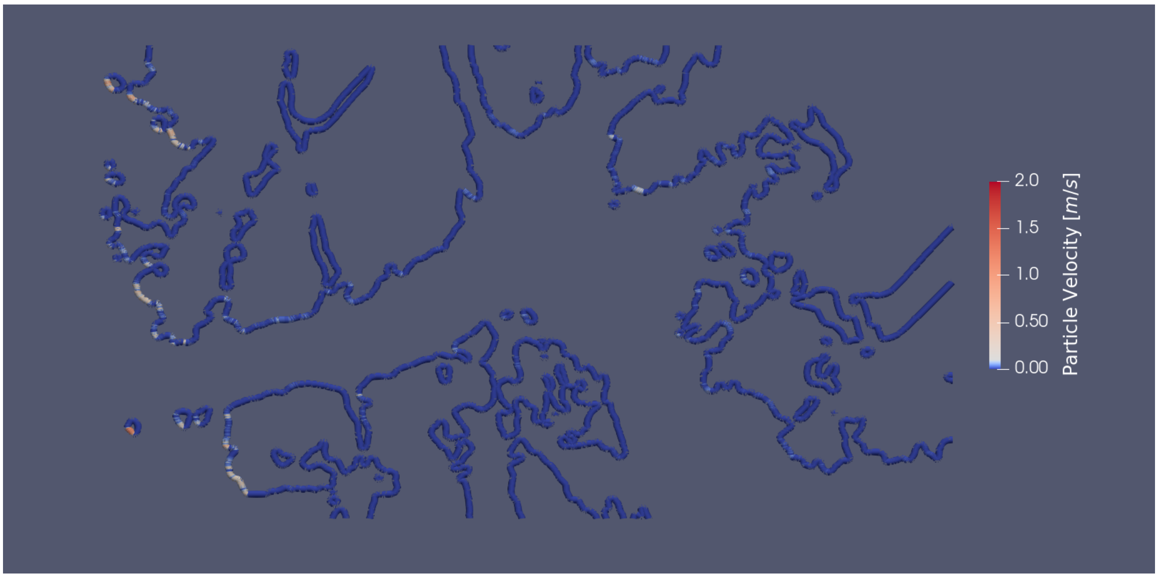

Figure 5.11: Particle velocity at the numerical coastline for a damping distance of 100 m.

150 m at the deepest. Nevertheless, significant reflection is evident all over the domain (see figure 5.11).

To increase the damping distance to 120 m results in some reflection. However, this is mainly in the outer coastline and is relatively small. At P3, there is a difference in the significant wave height of two percent between simulations with a damping distance of 120 m and 200 m. Additionally, the coastal relaxation zone is not unnecessarily extensive, which is visible in figure 5.15. Most of the numerical coastline remains in shallow water, although there are some small stretches where the energy is dissipated for depths up to 250 m.

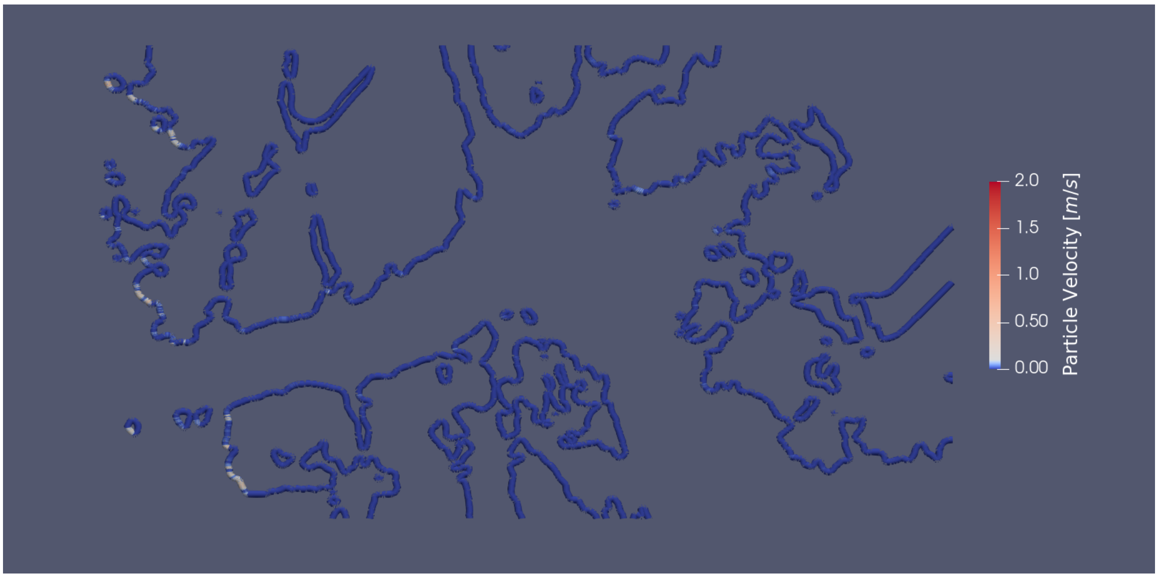

Figure 5.12: Particle velocity at the numerical coastline for a damping distance of 120 m.

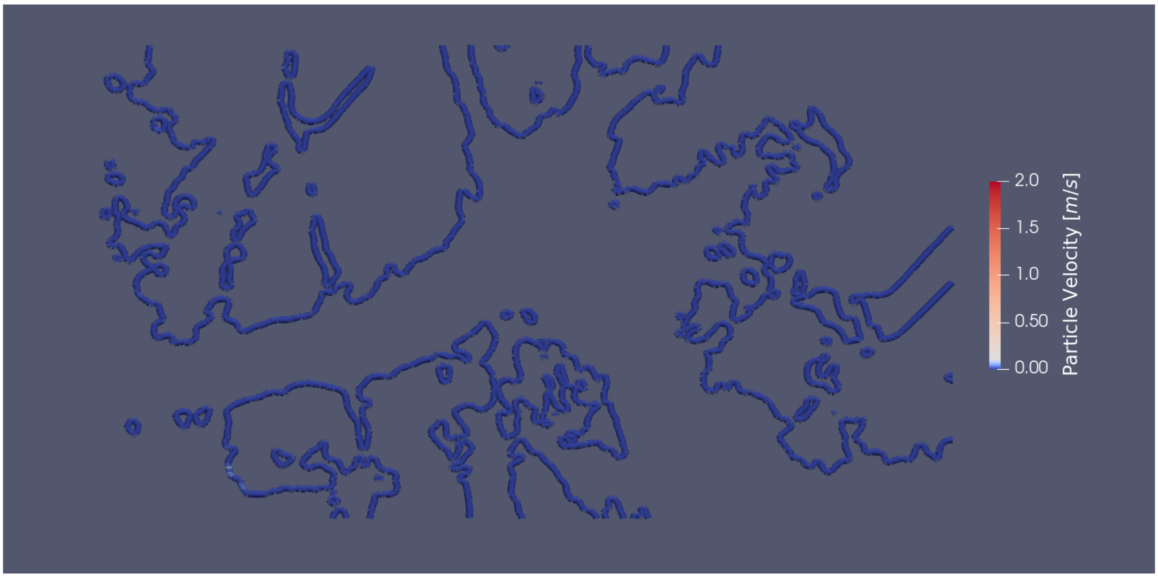

Figure 5.13: Particle velocity at the numerical coastline for a damping distance of 200 m.

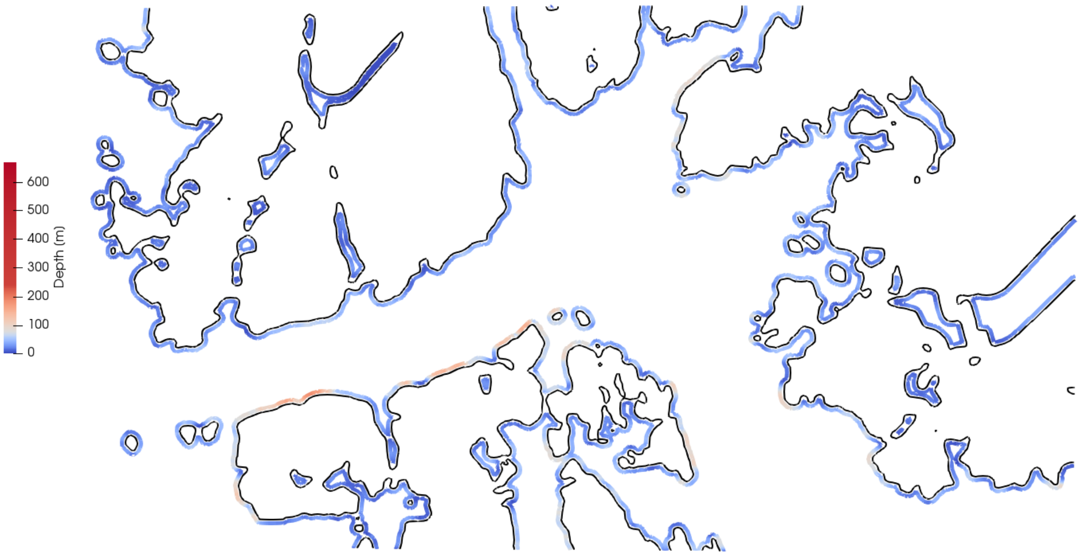

Figure 5.14: Depth at the start of the coastal relaxation zone. The coastline is represented by the black lines. Coastline damping distance = 100 m.

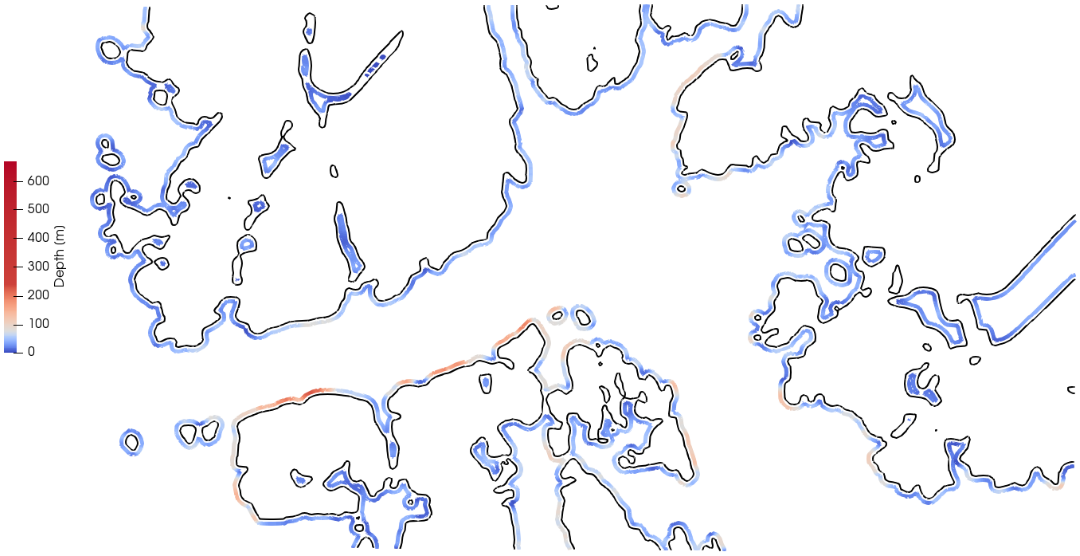

Figure 5.15: Depth at the start of the coastal relaxation zone. The coastline is represented by the black lines. Coastline damping distance = 120 m.

Figure 5.16: Depth at the start of the coastal relaxation zone. The coastline is represented by the black lines. Coastline damping distance = 200 m.

Chapter 6

Study of Wave Properties in Bjørnafjorden

The numerical domain is decomposed into a computational grid with a cell size of 25x25 meters in the horizontal directions, and ten cells in the vertical direction. The sigma-grid, with a vertical stretching factor of 2.5, determines the mesh size in the vertical direction. This grid resolution yields 25 200 000 cells. The CFL criterion is set to 1.0, which results in a constant time step of 0.309 seconds under these conditions. Combined with a simulated time of 12 800 seconds, the simulation will require an enormous number of calculations. The workload is therefore distributed across 256 processors, resulting in an average of 98 437 cells per processor. The supercomputer FRAM is used to conduct the simulations with the run time presented in table 6.1.

Wave Input 1 (0 degrees)	15 hrs, 56 min
Wave Input (45 degrees)	16 hrs, 28 min
Wave Input (315 degrees)	16 hrs, 35 min
Wave Input 2	15 hrs, 07 min
Wave Input 3	16 hrs, 26 min

Table 6.1: Run time of full-scale simulations.

Figure 6.1 shows that the incident waves are imposed at the western boundary (green box), while wave absorption zones (red boxes) are placed at the other boundaries to avoid unphysical reflection. Energy is also dissipated within the coastal relaxation zone that extends 120 m out from the coastline.

The location and identification of the 22 numerical wave gauges in the computational model are also illustrated in figure 6.1. Seventeen of these wave gauges are placed offshore and along both channels to see how the waves develop as they propagate towards Bjørnafjorden, while five of the wave gauges are placed in Bjørnafjorden to determine the wave conditions in the fjord.

The three different wave inputs presented in Section 4.2 are used in the full-scale modeling of Bjørnafjorden in different directions, resulting in five unique simulations. These wave properties are imposed as first-order irregular waves made up of 2048 regular waves. The individual wave periods are distributed according to the JONSWAP spectrum, with the corresponding peak shape parameter γ set to 3.3. The directional spreading of the incident waves is determined by the Mitsuyasu-type spreading function, with a shape parameter n of 80 and a sector of 180 degrees.

The results of these simulations are presented in the following sections. Comparisons to measured data and numerical results from phase-averaging models are also presented. Additionally, simulations with the phase-averaging wave model SWAN are conducted in this study to complement the data presented by Aarnes [1]. The work by Aarnes involved simulations with real hindcast data as wave input. So the purpose of including simulations with SWAN in this work is to have more comparable simulations with the same wave input. The wave state is calculated with a spatial resolution of 150 m, 35 frequency bands, and 36 directional sectors, which is equal to the simulations presented by Aarnes.

6.1 Numerical Results

One of the advantages of using phase-resolving wave models compared to phase-averaging wave models is that each wave component is solved explicitly and hence providing more informative visualizations. The wave propagation for the different incident wave angles is presented in figures 6.2, 6.3, and 6.4. As one would expect, the waves propagate through the northern channel and the southern channel. The change in wave direction is distinct around Kyrholmen in the northern channel. The energy of these waves is concentrated towards the location of P18 and P19 due to refraction and diffraction.

On the other hand, waves from the southern channel are hardly visible in Bjørnafjorden. Even though the curve of the propagating waves in the southern channel is more gentle than in the northern channel, the energy is dissipated more significantly. One reason is the obstruction due to small islands and protruding parts of the land. Another reason is the water depth. In the northern channel, the gradient close to the

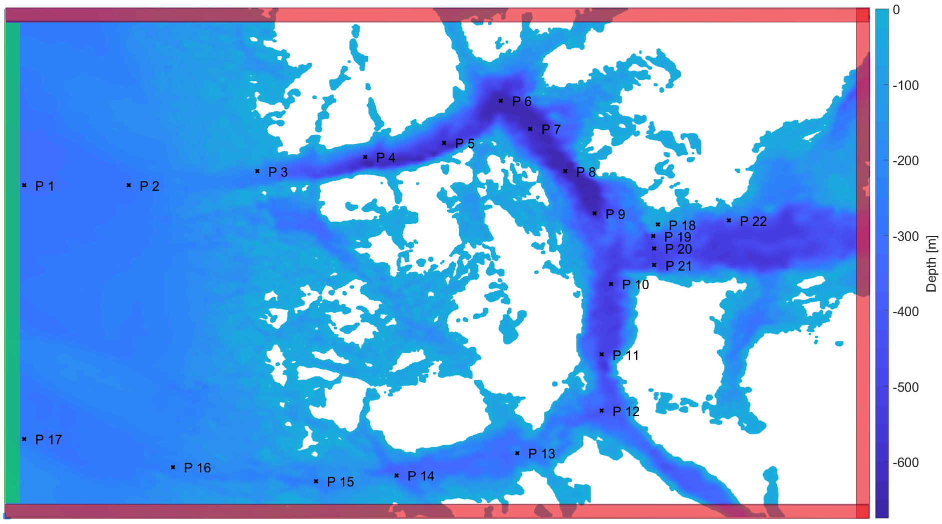

Figure 6.1: Illustration of the numerical domain, wave generation zone, wave absorption zones, and wave gauges (P1 - P22).

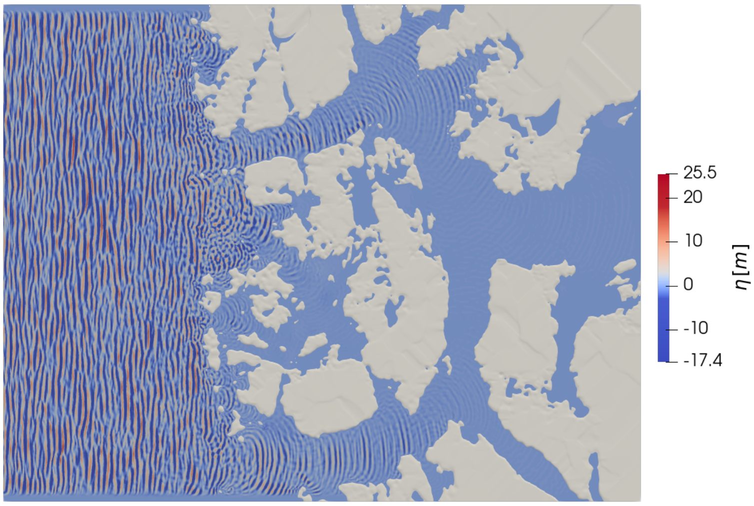

Figure 6.2: Free surface elevation in the domain for Wave Input 1 with the main wave direction of 0 degrees. Simulated time: 10 000 seconds.

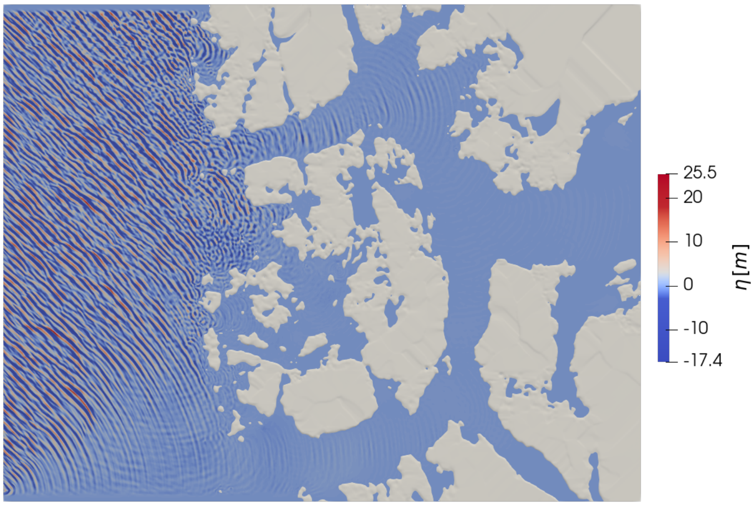

Figure 6.3: Free surface elevation in the domain for Wave Input 1 with the main wave direction of 45 degrees. Simulated time: 10 000 seconds.

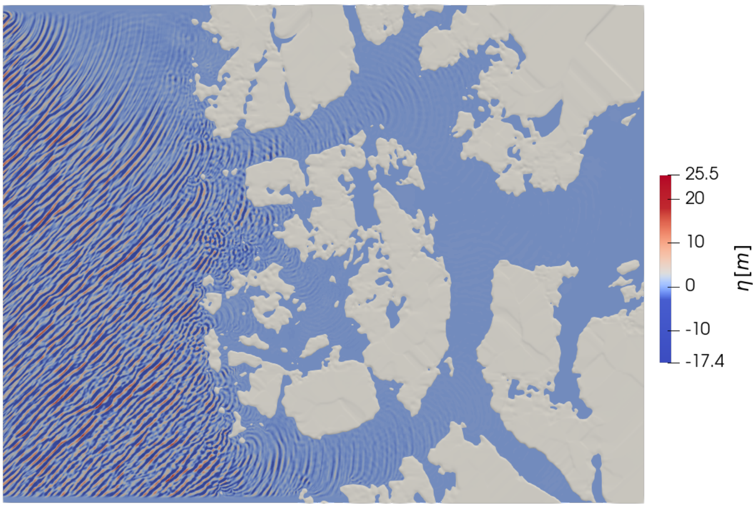

Figure 6.4: Free surface elevation in the domain for Wave Input 1 with the main wave direction of 315 degrees. Simulated time: 10 000 seconds.

shoreline is sharp, and the water is deep in the fjord, causing little wave-seabed interaction. However, in the southern channel, the water is shallower, resulting in more wave-seabed interaction. Waves are refracted towards the even shallower water, and the coastline, where the energy is dissipated.

The shallow water area of the southern channel could also cause low-frequency waves to decompose into smaller wave components. This process, and the capability of REEF3D to replicate it, is investigated by Bihs et al. [11].

It takes approximately 30 minutes for the waves to propagate from the offshore location to Bjørnafjorden.

Figure 6.3 illustrates a weakness of this study; when imposing an incident wave direction of 45 degrees, the waves will not directly propagate towards the inlet of the southern channel. To overcome this challenge, a domain that extends further south is needed. However, figure 4.6 indicates that the most severe wave conditions are because of waves propagating from the west or northwest. For an incident wave angle of 315 degrees, the domain area is sufficient.

As stated in Section 5.3, some reflection in the outer parts of the coast is expected in the simulation. These reflected waves propagate in a north-south direction, or a westerly direction, and are especially visible in the less disturbed offshore areas of the domain in figures 6.3 and 6.4. An alternative simulation with more extensive damping to avoid reflection is computed to check the impact of these reflected waves, and the difference in wave height at P1, P2, P16, and P17 is approximately four percent. This effect is therefore considered neglectable in this study due to the direction and the small wave height.

6.1.1 Northern Channel

The significant wave height in the northern channel for different incident wave directions is presented in figure 6.5. An incident wave angle of 45 (propagation from the southwest) or 315 degrees (propagation from the northwest) results in higher waves offshore (P1, P2, and P3). However, the inlets of the two channels are both facing west, consequently making waves entering the channels in from the west less obstructed. The significant wave height at P4 manifests this characteristic.

Figure 6.6 displays the significant wave height with a main incident wave direction of 0 degrees. The results for the similar simulations with SWAN are also presented.

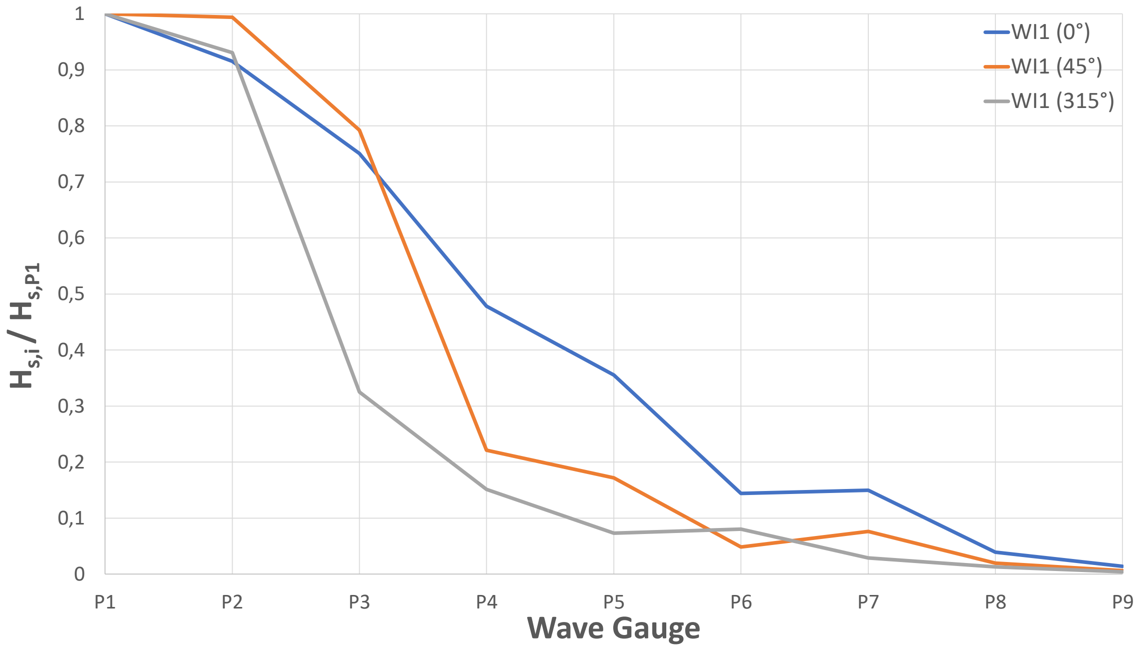

Figure 6.5: Northern channel. Relative significant wave height for Wave input 1 with different incident wave directions.

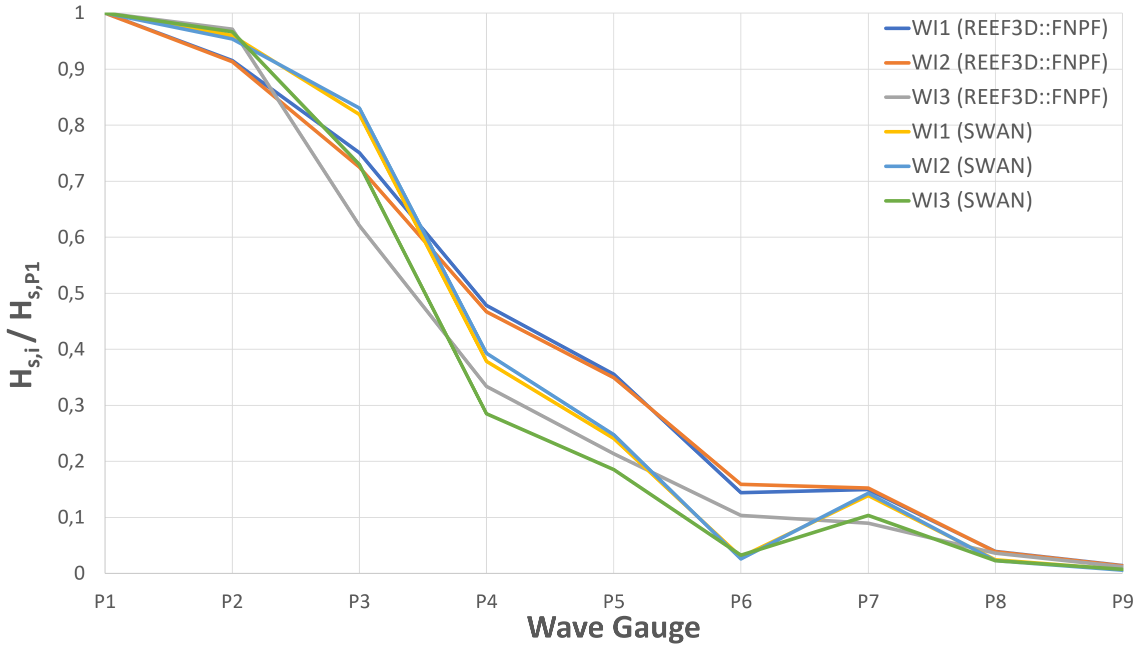

Figure 6.6: Northern channel. Relative significant wave height for different wave inputs with a wave direction of 0 degrees.

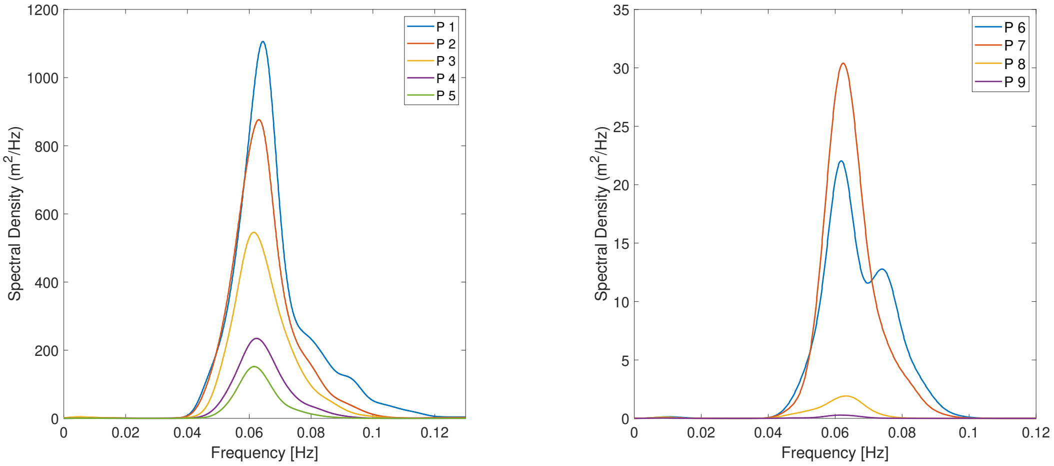

Figure 6.7: Northern channel. Wave spectra for Wave Input 1.

The findings of REEF3D shows that the wave heights of WI1 and WI2 are reduced the most at the inlet (between P3 and P4) and close to Kyrholmen (between P5 and P6/P7) while the wave height of WI3 is significantly reduced at the entrance of the channel.

When comparing the results of REEF3D and SWAN, the deviations are significant. In the offshore region, SWAN tends to calculate higher waves than REEF3D. Inside the fjord, the energy of the waves is dissipated more extensively for SWAN resulting in smaller waves. However, the results at P7 match to some extent for all three wave inputs. While REEF3D estimates approximately the same wave height at P6 and P7, SWAN calculates the wave height at P7 to be almost ten times as high as P6.

Recall from Section 5.2 that there will be some numerical dispersion in the model. Nevertheless, this is reduced to a minimum for this domain. Over a distance of ten kilometers, the wave phase is shifted by a maximum of one-fourth of the wavelength, according to figures 5.7, 5.8, and 5.9. However, with the varying depth, the amount of numerical dispersion will change over the domain. The waves in the domain are phase-shifted by a wavelength every 40 kilometers, as a conservative approximation. Given the longest wave input (WI3) at 680 m, the artificial change of a wavelength due to numerical dispersion will be 11.5 m or a change of 1.7 percent in wavelength from the wave generation zone to P22, assuming that this distance is 40 kilometers. The error might be even smaller when considering wave frequency. The simplified reason is that the relationship between the wave period and wavelength is ranging from proportional to quadratic depending on the water depth, according to linear wave theory. Hence, the artificial phase-shift due to the numerical dispersion is neglectable.

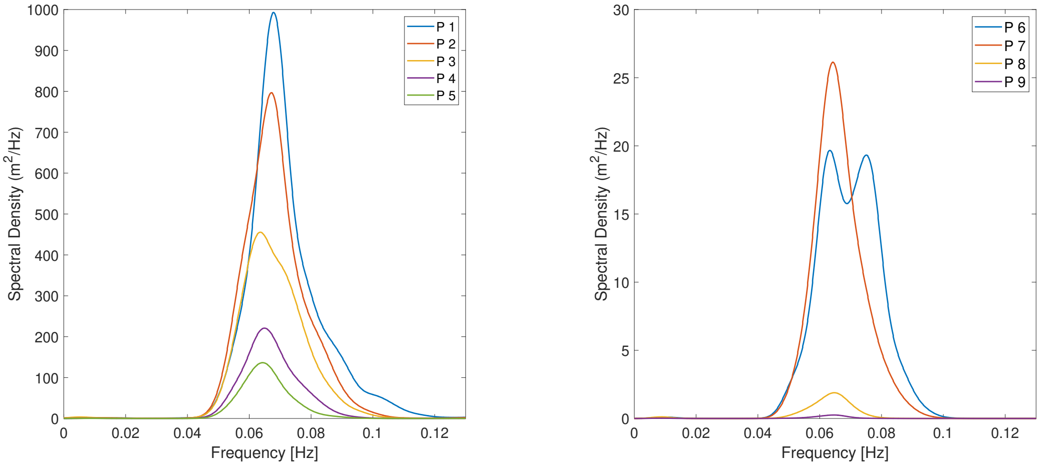

Figure 6.8: Northern channel. Wave spectra for Wave Input 2.

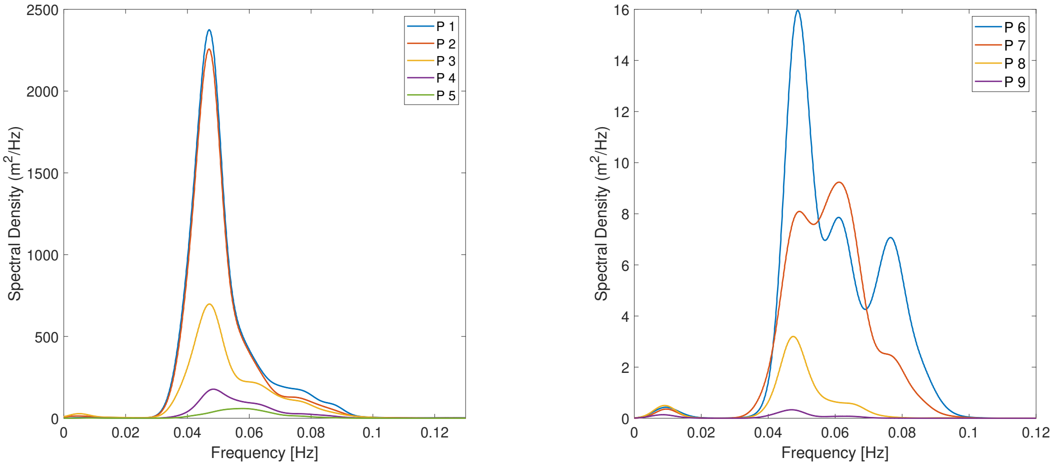

Figure 6.9: Northern channel. Wave spectra for Wave Input 3.

The development of the wave spectra for WI1 (figure 6.7) and WI2 (figure 6.8) is similar; the frequency distribution remains unchanged, and the energy is reduced as the waves propagate through the northern channel. However, there is a small deviation at P6. As the waves turn northwards, there is some tendency of energy moving to higher frequencies. This effect is more significant for WI2, which in general consists of smaller waves than WI1.

The redistribution of energy is even more significant for the longer waves of WI3 (figure 6.9). At P6, a notable amount of energy is redistributed to waves of almost twice as high frequency as the input frequency. The development of energy in waves with a frequency of approximately 0.01 Hz is another noteworthy characteristic of figure 6.9.

The sharp bend in the northern channel acts as a filter for higher frequency waves in Bjørnafjorden. The reason why the energy of higher frequencies are heavily reduced in P8 and P9 is that the refraction and diffraction process is more substantial for longer waves. That is why the shorter waves strongly influence the wave spectra at P6 and partly P7, but not at P8 and P9.

6.1.2 Southern Channel

Figure 6.10 presents a comparison of the wave height from different incident wave directions in the southern channel. Similar to the northern part, it is evident that waves that are coming from the southwest and the northwest result in smaller waves in the fjords, compared to waves propagating from the west. However, due to the constraints of the domain and the model configuration, the waves coming from the southwest will not directly propagate towards the southern channel. Waves are only imposed on the western boundary of the numerical domain, and with an incident wave angle of 45 degrees, only diffracted waves will reach the inlet of the southern channel. The wave propagation is visible in figure 6.3. To correctly analyze the influence of waves coming from the southwest, the domain needs to be extended in the southern direction.

For waves coming from the west (figure 6.11), the reduction in significant wave height is more evenly distributed in the southern channel than in the northern channel. Nevertheless, the wave heights of WI3 are significantly reduced at the inlet of the fjord, between P16 and P15. A considerable amount of these long waves are probably refracted towards the shoreline due to the relatively shallow water. Although REEF3D and SWAN provide very similar results for WI3, SWAN does not capture this feature.

For WI1 and WI2, the wave heights calculated by SWAN are, in general, smaller than what is estimated by REEF3D. The same trend is evident for the northern channel.

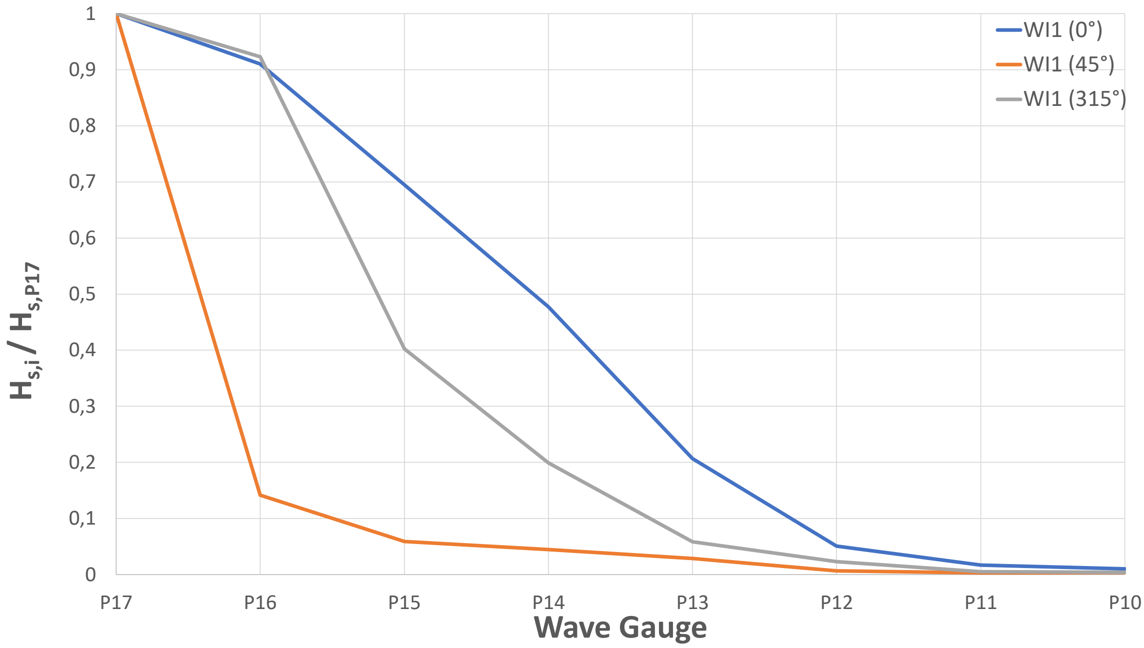

Figure 6.10: Southern channel. Relative significant wave height for Wave input 1 with different incident wave directions.

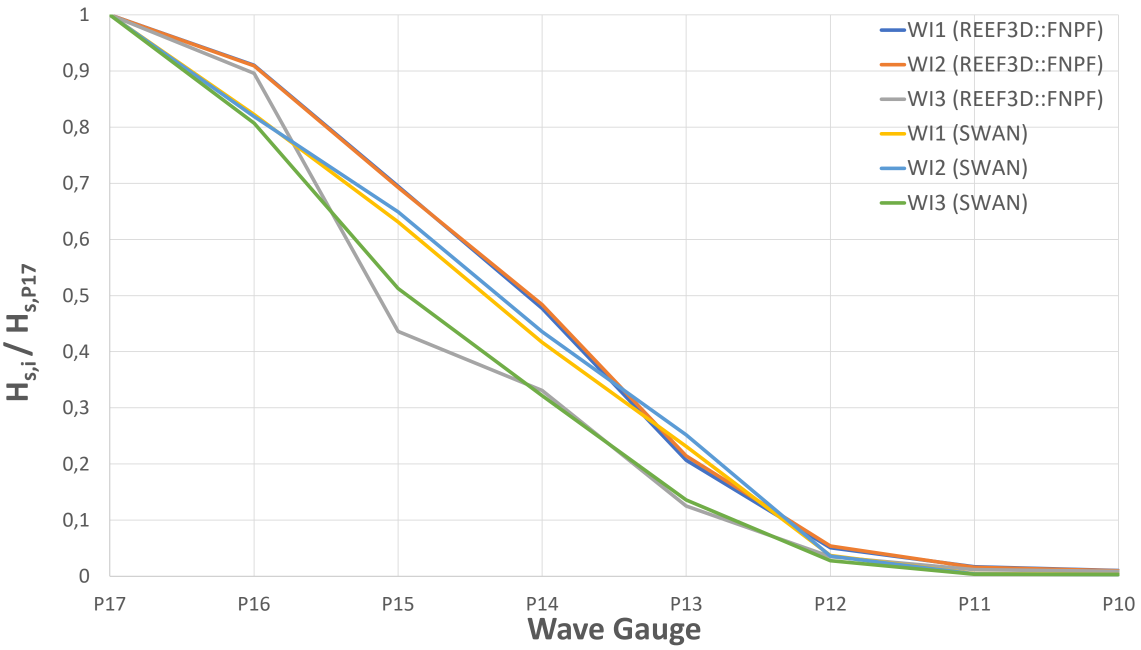

Figure 6.11: Southern channel. Relative significant wave height for different wave inputs with a wave direction of 0 degrees.

Evaluating WI1 and WI2 (figure 6.12 and 6.13), the distribution of wave frequency appears unchanged offshore and in Selbjørnsfjorden (P15-P13), except for the dissipation of wave energy. However, for WI3 (figure 6.14), the distinct peak frequency is lost as the wave energy is spread over a wider band of frequencies when the waves enter the shallow inlet of Selbjørnsfjorden. As the waves propagate into Langenuen (P12-P10), a peak in the frequency spectrum develops slightly below 0.01 Hz. This peak in the frequency spectrum is particularly dominant in the results for WI3.

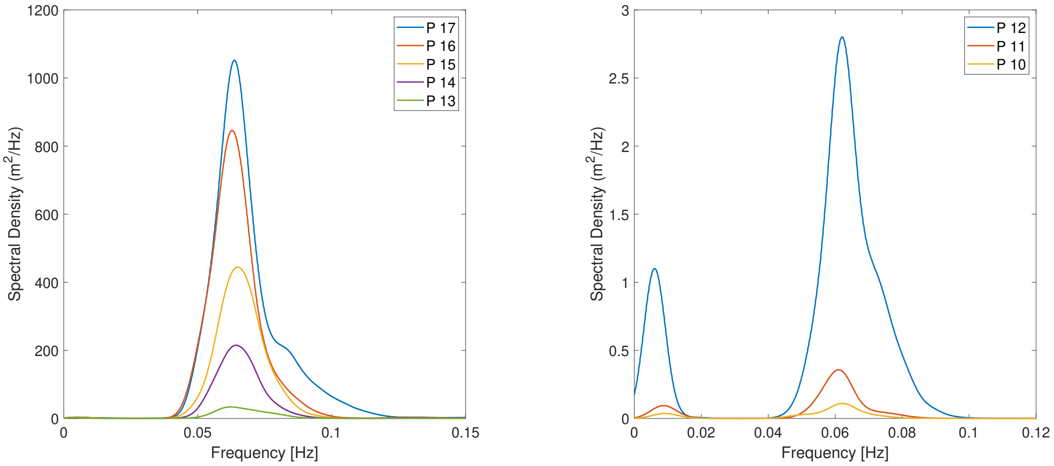

Figure 6.12: Southern channel. Wave spectra for Wave Input 1.

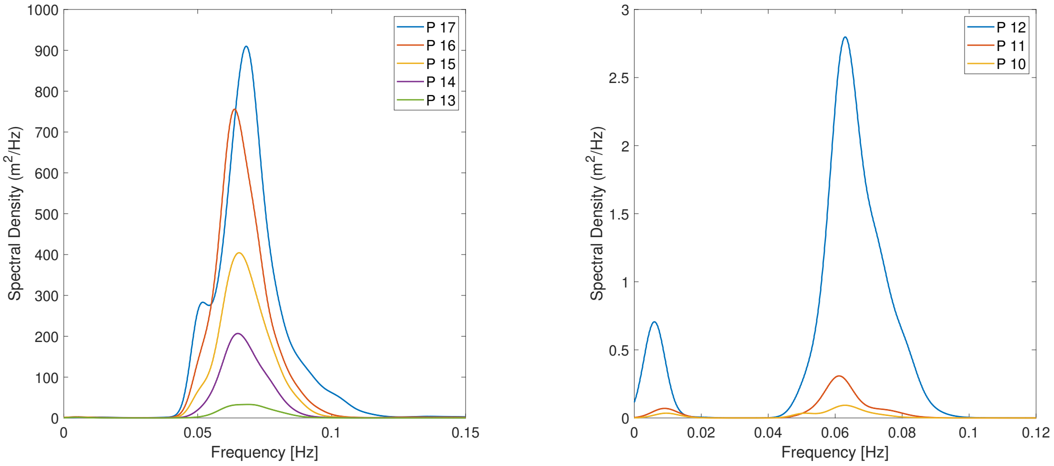

Figure 6.13: Southern channel. Wave spectra for Wave Input 2.

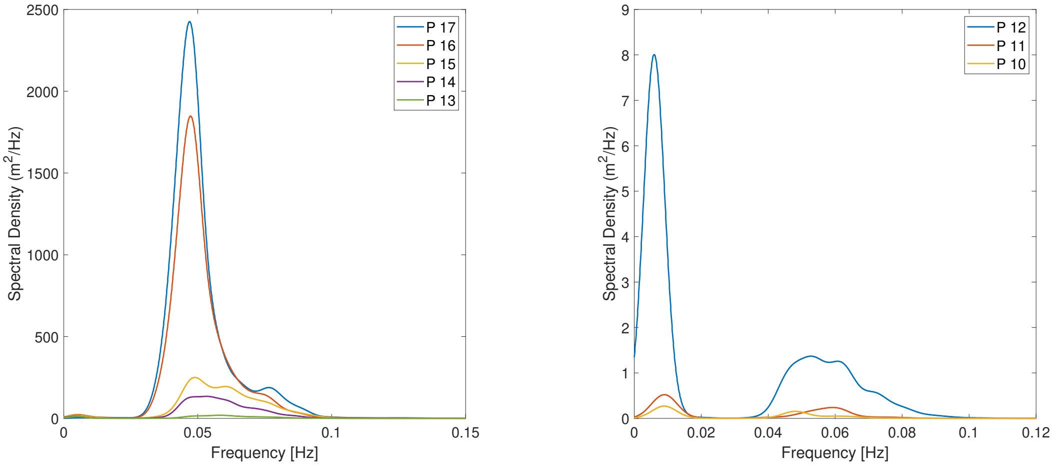

Figure 6.14: Southern channel. Wave spectra for Wave Input 3.

6.1.3 Bjørnafjorden

Long waves with a frequency of approximately 0.01 Hz are also present in Bjørnafjorden for all three wave inputs, although the energy of these wave components is low (see figures 6.15, 6.16, and 6.17). More interestingly is the fact that these wave components are not apparent in the results from SWAN despite being in the frequency domain of the SWAN simulation. Since REEF3D::FNPF is the wave model with fewer simplifications, it is reasonable to assume that the deficiency lies with SWAN, which is not able to replicate these wave components.

In general, the dominating wave frequencies at approximately 0.06 Hz are captured by both wave models. However, for all cases, SWAN seems to underestimate the wave energy at P19, especially. One explanation is that the waves propagate over bathymetry with a steep gradient, before reaching P19. Over a horizontal distance of approximately 300 m, the water depth changes from 140 m to 378 m. Phase-averaging models, like SWAN, are not as accurate for rapidly varying conditions, such as the depth at this location.

The significant wave heights for the wave gauges in Bjørnafjorden, presented in table 6.2, illustrates the same tendency at P19. Additionally, the other wave gauges show the same outcome; the significant wave heights calculated by SWAN are smaller than the calculations by REEF3D.

The significant wave heights calculated by REEF3D varies from 14 cm at P22 to 58 cm at P18, where shoaling is evident. The depth at this location is 49 m, which causes the waves to slow down and the wave height to increase. It seems reasonable that the wave heights for WI3 are higher than the two other wave inputs. However, that is not the case for P18. When evaluating figure 6.17, it seems like a larger share of the energy is redistributed to the lower frequencies compared to the other two wave inputs. This effect is especially evident for P10 and P18, where also the difference in significant wave height is smaller than at most of the wave gauges (see table 6.2).

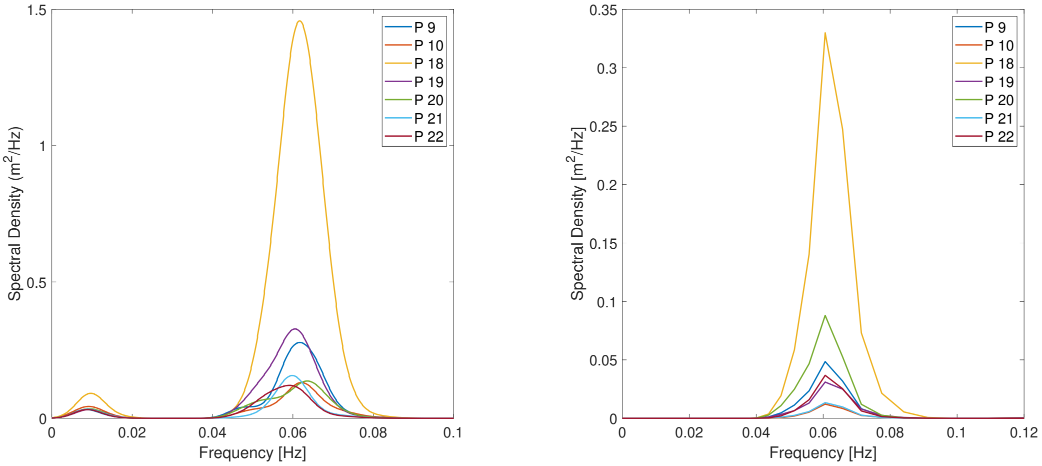

Figure 6.15: Wave spectra in Bjørnafjorden calculated by REEF3D::FNPF (left) and SWAN (right) for Wave Input 1.

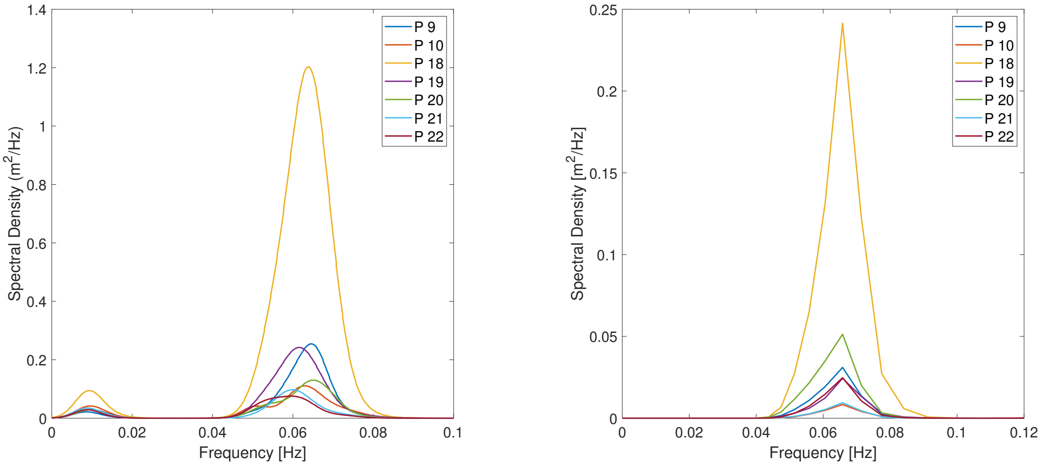

Figure 6.16: Wave spectra in Bjørnafjorden calculated by REEF3D::FNPF (left) and SWAN (right) for Wave Input 2.

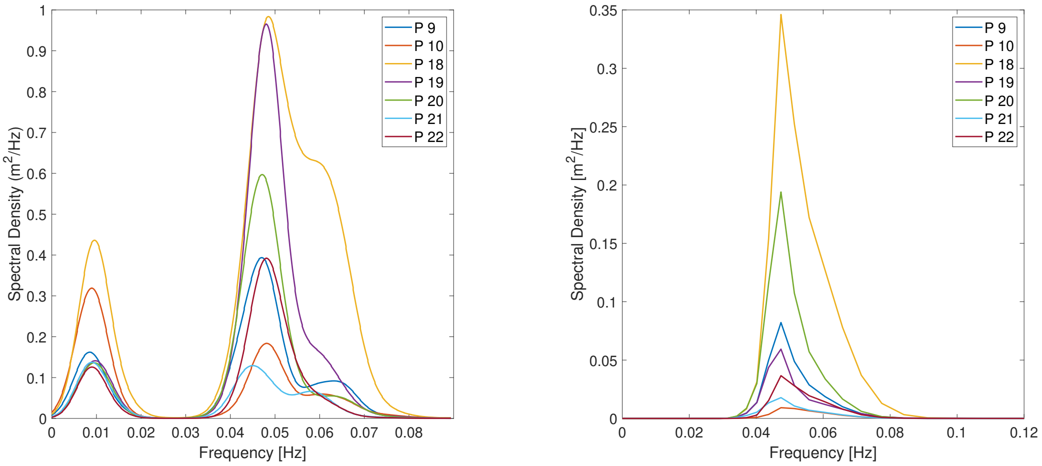

Figure 6.17: Wave spectra in Bjørnafjorden calculated by REEF3D::FNPF (left) and SWAN (right) for Wave Input 3.

	REEF3D::FNPF			SWAN		
	Wave Input 1	Wave Input 2	Wave Input 3	Wave Input 1	Wave Input 2	Wave Input 3
P9	0.25 m	0.23 m	0.28 m	0.10 m	0.08 m	0.13 m
P10	0.18 m	0.17 m	0.21 m	0.05 m	0.04 m	0.05 m
P18	0.58 m	0.54 m	0.55 m	0.27 m	0.23 m	0.29 m
P19	0.28 m	0.24 m	0.41 m	0.09 m	0.07 m	0.11 m
P20	0.19 m	0.18 m	0.32 m	0.14 m	0.11 m	0.19 m
P21	0.17 m	0.15 m	0.18 m	0.05 m	0.05 m	0.07 m
P22	0.17 m	0.14 m	0.26 m	0.09 m	0.07 m	0.09 m

Table 6.2: Significant wave height in Bjørnafjorden.

6.2 Discussion of the Results

6.2.1 Discussion of the Results

In the study by Aarnes [1], simulations with a phase-averaging wave model are presented to evaluate the wave conditions in Bjørnafjorden because of swell waves. The computed significant wave height for a 100-year return period is 3 cm in the middle of the proposed fjord crossing, close to P20. The swell waves are imposed offshore at the western boundary and are based on 15 years of wave measurements. The significant wave height is statistically calculated. However, these results are compared to measurements that indicate a significant wave height of approximately 30 cm for a return period of 100 years is to be expected in Bjørnafjorden. The conclusion in this study is that SWAN attenuates swell too efficiently propagating into the fjord. This outcome is also evident in this study when comparing REEF3D and SWAN in table 6.2.

Cheng et al. [17] also analyze wave measurements from Bjørnafjorden. The dataset contains 27 024 samples from 19 months. There were 11 occasions where the wave height surpassed 30 cm, and the wave period exceeded seven seconds. These measurements indicate that the significant wave height for swell waves should be well above 30 cm for a return period of 100 years. The location of these measurements was approximately at P19 and P20.

The significant wave height of 40 cm, calculated by Norconsult and presented in the design basis for the fjord crossing [45], might be a more accurate estimate. However, the value is assumed to be constant across the fjord due to a lack of adequate data, which raises some concerns about the validity of the estimation.

Based on the results from both REEF3D and SWAN (see table 6.2), it is evident that shoaling occurs at P18 and P19, which corresponds to almost one-third of the fjord crossing. This physical process results in twice as high waves for the northern part of the fjord crossing. So, to assume a constant significant wave height across the fjord appears inaccurate.

Measurements in Bjørnafjorden shows that the wave height is reduced by approximately ten percent between P19 and P20 [17]. The results for REEF3D shows the same tendency between these two locations, but with a magnitude of approximately 25 percent. However, these measuring points are not in identical positions, and small changes in the location could cause significant changes in the water depth, especially with the rapidly varying water depth around P19. SWAN, on the other hand, consistently calculate higher waves at P20 than P19. This deviation is due to rapidly varying water depth, as discussed earlier.

Compared to the significant wave heights presented in this section, the results from REEF3D appears to be of the same magnitude. Phase-averaging wave models, like SWAN and STWAVE, often struggle when the conditions are quickly varying, making the calculations of, among other physical processes, refraction and diffraction less accurate. These processes are particularly critical for wave propagation in Norwegian fjords and might be the reason for the deviations in the results. Based on the simulation with Wave Input 1, where the offshore significant wave height for a 100-year return period is simulated, the significant wave height at the fjord crossing is ranging from 17 cm to 58 cm. The wave height could potentially be even higher closer to the shore than P18. The H_s at P20, calculated by REEF3D, are smaller than the measured data, which are given for a location close to P20. A too extensive coastal damping zone might be the reason.

The distribution of energy for different frequencies of swell waves is not illustrated in the studies presented in this section, which is understandable since the importance of swell waves in Bjørnafjorden is small compared to wind-generated waves. This type of wave is the main focus of these studies. However, the results from the phase-averaging simulation in this study show that SWAN is struggling to capture low-frequency waves that develop in the domain.

All the studies indicate that the impact of the northern channel is more significant than the southern channel, with the simulation by REEF3D revealing that 80 to 85 percent of the wave energy is coming from the northern channel. This value coincides with the results presented in the design basis [45].

6.2.2 Inhomogeneity at Fjord-Crossing Locations

It is common to assume homogeneous wave conditions across a fjord, meaning that the wave parameters are constant, yet this is often not the case in reality. Measurements in Bjørnafjorden [17] reveal that the wave parameters are varying along the proposed fjord crossing. The simulations by REEF3D show the same trend; the wave heights (see table 6.2) and the distribution of wave frequencies (see figures 6.15, 6.16, and 6.17) in the fjord are different to some degree. Particularly the longer waves of WI3 result in inhomogeneous wave conditions. The inhomogeneity of the wave conditions is an essential aspect since it is shown that inhomogeneous waves result in larger sway motion, axial force, and strong axis bending moment, together with significantly increased weak axis bending along the bridge girder compared to homogeneous wave conditions [16].

As illustrated by the introduced wave spectra, the wave energy is spread out over a broader band of frequencies in Bjørnafjorden compared to an offshore location. Still, the peak wave periods are quite distinct in Bjørnafjorden. The peak period along the proposed fjord crossing ranges from 15.5 seconds to 16.7 seconds for WI1 and WI2, and from 20.4 seconds to 22.2 seconds for WI3. Additionally, waves with a period of approximately 100 seconds are apparent in Bjørnafjorden for all wave inputs. In the design of floating structures, these wave periods are used to check if they match the eigenfrequencies of the structure, which could cause resonance. The first five eigenfrequencies of the proposed bridge design are 56.72, 31.69, 22.68, 18.62, and 14.33 seconds [15], which implies that none of the wave conditions investigated in this study will excite any of the modes of the proposed bridge. Nevertheless, the swell waves might be relevant for other aspects of the bridge design, like fatigue calculations.

Although the influence of swell waves is relatively small, it could coincide with wind from the west or the northwest direction, resulting in an amplified effect. This scenario is likely to occur since one of the two longest fetch distances in the fjord is along the line of P6, P7, P8, and P9, and measurements reveal that the dominating direction for wind waves in Bjørnafjorden are from the northern channel [17].

Chapter 7

Conclusion and Outlook

7.1 Summary

The main goal of this thesis is to simulate the swell wave conditions in Bjørnafjorden with the phase-resolving wave model REEF3D and to test the results against other wave models and measured data. The theoretical basis and the basic concepts of the fully nonlinear potential flow model are presented in Chapter 2 and Chapter 3. Before the large-scale simulations are calculated, the different input parameters are established to ensure the fidelity of the simulations. Initially, offshore wave parameters are determined to get realistic wave inputs used in the verification of the model, and the large-scale simulation. These wave inputs are used in a two-dimensional grid convergence study, with both constant depth and varying bathymetry, to obtain the necessary grid size in the horizontal plane, and the amount of grid stretching in the vertical direction. Furthermore, three-dimensional numerical simulations of Korsfjorden was used to determine the optimal coastline damping distance.

During the validation of the numerical model, it is observed that a horizontal grid size of 25 meters in both horizontal directions gives accurate results, with an error in the wave amplitude of approximately one percent. The numerical dispersion in the model is reduced to a neglectable amount with the implementation of vertical stretching of the grid. A vertical stretching factor of 2.5 with a focal point at the free surface yields an artificial phase-shift of the waves below 1.7 percent of the theoretical value. Finally, the coastline damping distance is set to 120 meters to optimize diffraction and reduce the unphysical dissipation and reflection of wave energy.

In the large-scale simulations of Bjørnafjorden, different incident wave angles are evaluated. These simulations show that waves with the main direction from the west cause the most severe waves in the fjords, even though the simulation with waves coming from the southwest was hampered due to the restrictions of the domain. The northern channel affects the wave conditions in Bjørnafjorden more than the shallow waters of the southern channels, which is in agreement with all available studies. The simulations with Wave Input 1 is emphasized in this study since it is based on the significant wave height for a return period of 100-years on an offshore location.

Besides the large-scale simulations with REEF3D, additional simulations with SWAN are performed. These simulations are performed with the same configurations as Aarnes [1] to complement the data presented in his study. The only difference is the wave input, which is identical to the ones used in the simulations with REEF3D.

The simulations with REEF3D show that swell waves with significant wave height up to 0.58 meters are apparent in Bjørnafjorden. SWAN, on the other hand, predicts a maximum wave height of 0.27 meters for the same offshore wave input. Nevertheless, some of the other studies indicate that phase-averaging wave models underpredict the wave height, which is reasonable given that these are the less demanding models of the two types of wave models. Data from field measurements for 19 months present several data points with waves higher than 0.3 meters, which indicates that the significant wave height for a 100-year return period is well above the 27 centimeters proposed by SWAN, and it strengthens the statement that SWAN underestimates the wave conditions. Even though it is stated that parts of the simulation are inadequate, it is worth noticing that simulations with STWAVE calculated a significant wave height of 40 centimeters in Bjørnafjorden [45].

Both types of models show agreement when it comes to the development of the wave spectra at the peak frequency. In the northern channel, the shorter wave components are filtered out by the sharp curve since diffraction and refraction are more significant for longer waves. Whereas in the southern channel, wave spectra calculated by REEF3D indicates that energy is redistributed to waves at a frequency of approximately 0.01 Hz. SWAN, on the other hand, does not capture these low-frequent wave components.

Finally, the wave conditions in Bjørnafjorden is found to be inhomogeneous, which implies that the design wave parameters are varying across the fjord. However, it is assumed homogeneous wave conditions in the design basis of the proposed fjord crossing [45], even though the study by Chen [16] found it to be a nonconservative assumption.

7.2 Conclusion

Large-scale simulations have successfully been simulated with the phase-resolving wave model REEF3D::FNPF to explore the wave conditions in Bjørnafjorden. The quickly varying bathymetry of this fjord is a challenge for numerical wave models, yet this wave model is proven to be stable and relatively efficient.

The numerical model is verified through several two- and three-dimensional simulations. The necessary grid resolution is found to be 25 meters in both horizontal directions, while a nonuniform sigma-grid with ten cells is used in the vertical direction. A coastline damping distance of 120 meters is found to be the minimum distance to avoid the unphysical reflection that will corrupt the results. Despite being significantly more computationally demanding than phase-averaging models, this numerical model requires a computation time below 17 hours on 256 processors, which is relatively efficient.

The significant wave height with a 100-year return period is calculated by REEF3D::FNPF to be 0.58 meters for swell waves, which is approximately one-fifth of the corresponding wave height for wind-generated waves. Even though the influence from swell waves in Bjørnafjorden is small compared to wind-generated waves, co-occurrence with the same direction is an anticipated event, and so cannot be neglected in Bjørnafjorden. Additionally, the comparison to measured data shows better agreement with results from REEF3D::FNPF than results from SWAN, which support the claim that phase-averaging wave models are underestimating the wave heights. The phase-average models also struggle to replicate the low-frequent wave components that are generated in the southern channel.

This thesis illustrates the capability of phase-resolving models, exemplified by REEF3D::FNPF, and proves that these models are significant upgrades from phase-averaging wave models, provided that the necessary computational resources are available and that the wind-generated waves are also considered.

7.3 Outlook

This study illustrates several of the advantages by using phase-resolved wave models compared to phase-averaging wave models. With the increased utilization of the ocean space and the expected extreme weather due to global warming, environmental forces, like wave forces, are of increased importance in the design process of marine structures. Consequently, resulting in an increased demand for more accurate numerical models, which could result in high demand for well-developed phase-resolved wave models for large-scale modeling in the future. Another factor is that computer resources are continuously becoming less costly, making the upgrade from phase-averaging to phase-resolving wave models less expensive.

Nevertheless, phase-resolving wave models are still relatively unproven for large-scale wave modeling, especially for challenging topography like the Norwegian coast. Further verification of the model is therefore needed. One possibility is to gather simultaneous wave data for an offshore and in-fjord location. The offshore wave data is used as input for the wave model, while the in-fjord data is used to check if the numerical model can replicate the wave propagation accurately.

One major disadvantage of the more advanced phase-resolved wave models is the lack of wind-generated waves in the domain. However, for REEF3D, this is expected to be implemented in the future. Another limitation of the numerical model is the dissipation of the energy at the coastline. The existing method raises the concern with a trade-off between unphysical damping and a reduced diffraction process, and artificial reflection. The development of an alternative method with a less extensive damping distance, which still can dissipate the energy sufficiently, will provide more accurate refraction and diffraction processes.

References

[1] Aarnes, O. J. Wave conditions in bjørnafjorden. Norwegian Meteorological Institute - Division for Oceanography and Marine Meteorology, 2019.

[2] A. Aggarwal, M. A. Chella, H. Bihs, C. Pákzodi, and A. Arntsen. Numerical study of wave transformation using the free surface reconstruction method. In *7th International Conference on Computational Methods in Marine Engineering, MARINE 2017*, volume 2017-May, pages 884–892, 2017.

[3] N. Ahmad, H. Bihs, A. Kamath, and A. Arntsen. Three-dimensional cfd modeling of wave scour around side-by-side and triangular arrangement of piles with reef3d. *Procedia Engineering*, 116(C):683–690, 2015.

[4] M. Alagan Chella, H. Bihs, D. Myrhaug, and M. Muskulus. Hydrodynamic characteristics and geometric properties of plunging and spilling breakers over impermeable slopes. *Ocean Modelling*, 103:53–72, 2016.

[5] F. Ardhuin, B. Chapron, and F. Collard. Observation of swell dissipation across oceans. *Geophysical Research Letters*, 36:L06607, 03 2009.

[6] A. Baquet, J. Kim, and Z. J. Huang. Numerical Modeling Using CFD and Potential Wave Theory for Three-Hour Nonlinear Irregular Wave Simulations. volume 1: Offshore Technology of *International Conference on Offshore Mechanics and Arctic Engineering*, 06 2017. V001T01A002.

[7] S. Beji and J. A. Battjes. Experimental investigation of wave propagation over a bar. *Coastal Engineering*, 19:151–162, 1993.

[8] S. Beji and J. A. Battjes. Numerical simulation of nonlinear wave propagation over a bar. *Coastal Engineering*, 23:1–16, 1994.

[9] H. Bihs. *Three-Dimensional Numerical Modeling of Local Scouring in Open Channel Flow.* PhD thesis, NTNU, Trondheim, Norway, 2011.

[10] H. Bihs, A. Kamath, M. Chella, and Arntsen. Extreme wave generation, breaking, and impact simulations using wave packets in reef3d. *Journal of Offshore Mechanics and Arctic Engineering*, 141(4), 2019.

[11] H. Bihs, W. Wang, C. Pakozdi, and A. Kamath. REEF3D::FNPF—A Flexible Fully Nonlinear Potential Flow Solver. *Journal of Offshore Mechanics and Arctic Engineering*, 142(4):1–12, 02 2020. 041902.

[12] L. Cavaleri. Wave modeling: Missing the peaks. *Journal of Physical Oceanography*, 39(11):2757–2778, 2009.

[13] D. Chalikov. *Phase-Resolving Wave Modeling*, pages 1–11. American Cancer Society, 2017.

[14] W. Chen, Z. Demirbilek, and L. Lin. Coupling phase-resolving nearshore wave models with phase-averaged spectral wave models in coastal applications. In *Proceedings of the International Conference on Estuarine and Coastal Modeling*, volume 388, pages 582–600, 2010.

[15] Z. Cheng, Z. Gao, and T. Moan. Hydrodynamic load modeling and analysis of a floating bridge in homogeneous wave conditions. *Marine Structures*, 59:122–141, 2018.

[16] Z. Cheng, Z. Gao, and T. Moan. Wave load effect analysis of a floating bridge in a fjord considering inhomogeneous wave conditions. *Engineering Structures*, 163:197–214, 2018.

[17] Z. Cheng, E. Svangstu, Z. Gao, and T. Moan. Field measurements of inhomogeneous wave conditions in bjørnafjorden. *Journal of Waterway, Port, Coastal, and Ocean Engineering*, 145(1):5018008, 2019.

[18] I. E. Davik. Numerical study on wave propagation in norwegian fjords for the e39 project. Project report, 2019.

[19] R. G. Dean and R. A. Dalrymple. *Water wave mechanics for engineers and scientists*. World Scientific, 1991.

[20] Delft University of Technology. *SWASH User Manual*, 2019.

[21] DNV. Modelling and analysis of marine operations DNV-RP-H103. Det Norske Veritas (DNV), Norway, 2011.

[22] D. G. Dommermuth and D. K. P. Yue. A high-order spectral method for the study of nonlinear gravity waves. *Journal of Fluid Mechanics*, 184:267–288, 1987.

[23] K. K. Dunham. Coastal highway route e39 – extreme crossings. *Transportation Research Procedia*, 14:494 – 498, 2016. Transport Research Arena TRA2016.

[24] M. R. Eldrup and T. L. Andersen. Numerical study on regular wave shoaling, deshoaling and decomposition of free/bound waves on gentle and steep foreshores. *Journal of Marine Science and Engineering*, 8(334):334, 2020.

[25] R. D. Falgout, J. E. Jones, and U. M. Yang. Pursuing scalability for hypre 's conceptual interfaces. *ACM Transactions on Mathematical Software*, 31(3):326–350, 2005.

[26] R. D. Falgout and U. M. Yang. *hypre: A Library of High Performance Preconditioners*, volume 2331. Springer Berlin Heidelberg, United States, 2002.

[27] J. D. Fenton. A fifth order Stokes theory for steady waves. *Journal of Waterway, Port, Coastal and Ocean Engineering*, 111(2):216–234, 1985.

[28] I. Grabemann and R. Weisse. Climate change impact on extreme wave conditions in the north sea: An ensemble study. *Ocean Dynamics*, 58(3-4):199–212, 2008.

[29] A. Harten. High resolution schemes for hyperbolic conservation laws. *Journal of Computational Physics*, 49:357–393, 1983.

[30] L. Holthuijsen. *Waves in oceanics and coastal waters.* Cambridge University Press, 2007.

[31] N. G. Jacobsen, D. R. Fuhrman, and J. Fredsøe. A wave generation toolbox for the open-source CFD library: OpenFOAM. *International Journal for Numerical Methods in Fluids*, 70(9):1073–1088, 2012.

[32] G. S. Jiang and D. Peng. Weighted ENO schemes for Hamilton-Jacobi equations. *SIAM Journal on Scientific Computing*, 21:2126–2143, 2000.

[33] G. S. Jiang and C. W. Shu. Efficient implementation of weighted ENO schemes. *Journal of Computational Physics*, 126:202–228, 1996.

[34] A. Kamath, H. Bihs, M. A. Chella, and Øivind A. Arntsen. Cfd simulations to determine wave forces on a row of cylinders. *Procedia Engineering*, 116:623 – 630, 2015. 8th International Conference on Asian and Pacific Coasts (APAC 2015).

[35] A. Kamath, M. Chella, R. Archetti, and H. Bihs. Analysis of different methods for wave generation and absorption in a cfd-based numerical wave tank. *Journal of Marine Science and Engineering*, 6(2), 2018.

[36] B. E. Launder and N. D. Sandham. *Closure Strategies for Turbulent and Transitional Flows.* Cambridge University Press, GB, 2002.

[37] B. Le Méhauté. *An introduction to hydrodynamics and water waves.* Springer-Verlag, New York, 1976.

[38] Z. H. Ma, L. Qian, D. M. Causon, H. B. Gu, and C. G. Mingham. A cartesian ghost-cell multigrid poisson solver for incompressible flows. *International Journal for Numerical Methods in Engineering*, 85(2):230–246, 2011.

[39] T. Martin and I. Shevchuk. Implementation and validation of semi-implicit weno schemes using openfoam®. *Computation*, 6(1):6, 2018.

[40] S. Mayer, A. Garapon, and L. S. Sørensen. A fractional step method for unsteady free surface flow with applications to non-linear wave dynamics. *International Journal for Numerical Methods in Fluids*, 28:293–315, 1998.

[41] M. McCabe, P. K. Stansby, and D. D. Apsley. Coupled wave action and shallow-water modelling for random wave runup on a slope. *Journal of Hydraulic Research*, 49(4):515–522, 2011.

[42] H. Mitsuyasu, F. Tasai, T. Suhara, S. Mizuno, M. Ohkusu, T. Honda, and K. Rikiishi. Observations of the directional spectrum of ocean wavesusing a cloverleaf buoy. *Journal of physical oceanography*, 5(4):750–760, 1975.

[43] Moe, M. *Introduksjon til bølger og bølgekrefter.* NTNU, Trondheim, Norge, 2005.

[44] NORSOK Standard N-003. Actions and action effects. Standards Norway, Norway, 2007.

[45] NPRA. Design basis metocean SBJ-01-C3-SVV-01-BA-001. The Norwegian Public Roads Administration (NPRA), Norway, 2017.

[46] S. Osher and J. A. Sethian. Fronts propagating with curvature- dependent speed: algorithms based on Hamilton-Jacobi formulations. *Journal of Computational Physics*, 79:12–49, 1988.

[47] D. Peng, B. Merriman, S. Osher, H. Zhao, and M. Kang. A PDE-based fast local level set method. *Journal of Computational Physics*, 155:410–438, 1999.

[48] W. Pierson. *Practical Methods for Observing and Forecasting Ocean Waves by Means of Wave Spectra and Statistics.* Hydrographic Office. U.S. Government Printing Office, Washington, D.C., the, 1955.

[49] M. Quezada, A. Tamburrino, and Y. Niño. Numerical study of the hydrodynamics of waves and currents and their effects in pier scouring. *Water (Switzerland)*, 11(11), 2019.

[50] E. Rusu and C. G. Soares. Modeling waves in open coastal areas and harbors with phase-resolving and phase-averaged models. *Journal of Coastal Research*, 29(6):1309–1325, 2013.

[51] S. V. Samiksha, P. Vethamony, V. M. Aboobacker, and R. Rashmi. Propagation of atlantic ocean swells in the north indian ocean: a case study. *Natural hazards and earth system sciences*, 12(12):3605–3615, 2012.

[52] A. Sasikumar, A. Kamath, O. Musch, H. Bihs, and Arntsen. Numerical modeling of berm breakwater optimization with varying berm geometry using reef3d. *Journal of Offshore Mechanics and Arctic Engineering*, 141(1), 2019.

[53] C. W. Shu and S. Osher. Efficient implementation of essentially non-oscillatory shock capturing schemes. *Journal of Computational Physics*, 77:439–471, 1988.

[54] M. Sussman, P. Smereka, and S. Osher. A level set approach for computing solutions to incompressible two-phase flow. *Journal of Computational Physics*, 114:146–159, 1994.

[55] H. van der Vorst. BiCGStab: A fast and smoothly converging variant of Bi-CG for the solution of nonsymmetric linear systems. *SIAM Journal on Scientific and Statistical Computing*, 13:631–644, 1992.

[56] W. Wang, A. Kamath, C. Pakozdi, and H. Bihs. Investigation of focusing wave properties in a numerical wave tank with a fully nonlinear potential flow model. *Journal of Marine Science and Engineering*, 7(10):375, 2019.

[57] B. J. West, K. A. Brueckner, R. S. Janda, D. M. Milder, and R. L. Milton. A new numerical method for surface hydrodynamics. *Journal of Geophysical Research: Oceans*, 92(C11):11803–11824, 1987.

[58] Z.-J. You. A close approximation of wave dispersion relation for direct calculation of wavelength in any coastal water depth. *Applied Ocean Research*, 30(2):113 – 119, 2008.

NTNU

Norwegian University of
Science and Technology